

20 Abstract

21 Aerosol hygroscopicity plays a vital role in aerosol radiative forcing. One key parameter
22 describing hygroscopicity is the scattering enhancement factor, $f(\text{RH})$, defined as the ratio of
23 the scattering coefficient at humidified relative humidity (RH) to its dry value. Here, we utilize
24 the $f(80\%)$ from ORACLES 2016 and 2018 airborne measurements to investigate the
25 hygroscopicity of aerosols, its vertical distribution, its relationship with chemical composition,
26 and its sensitivity to organic aerosol (OA) hygroscopicity over the South-East Atlantic (SEA)
27 Ocean during the biomass burning (BB) season.

28 We found that aerosol hygroscopicity remains steady above 2 km, with a mean $f(80\%)$ of
29 1.40 ± 0.17 . Below 2 km, aerosol hygroscopicity increases with decreasing altitude, with a mean
30 $f(80\%)$ of 1.51 ± 0.22 , consistent with higher values of BB [aerosol](#) hygroscopicity found in the
31 literature. The hygroscopicity parameter of OA (κ_{OA}) is retrieved from the Mie model with a
32 mean value of 0.11 ± 0.08 , which is in the middle to upper range compared to literature. Higher
33 OA hygroscopicity is related to aerosols that are more aged, oxidized, and present at lower
34 altitudes. The enhanced BBA hygroscopicity at lower altitudes is mainly due to a lower OA
35 fraction, increased sulphate fraction, and greater κ_{OA} at lower altitudes.

36 We propose a parameterization that quantifies $f(\text{RH})$ with chemical composition and κ_{OA} based
37 on Mie simulation of internally mixed OA-(NH₄)₂SO₄-BC mixture. The good agreement
38 between the predictions and the ORACLES measurements implies that the aerosols in the SEA
39 during the BB season can be largely represented by the OA-(NH₄)₂SO₄-BC internal mixture
40 with respect to the $f(\text{RH})$ prediction. The sensitivity of $f(\text{RH})$ to κ_{OA} indicates that applying a
41 constant κ_{OA} is only suitable when the OA fraction is low and κ_{OA} shows limited variation.
42 However, in situations deviating these two criteria, κ_{OA} can notably impact scattering

43 coefficients and aerosol radiative effect; therefore, accounting for κ_{OA} variability is
44 recommended.

45 **Keywords:** hygroscopicity, biomass burning aerosol, chemical composition, κ_{OA} , Atlantic,
46 airborne measurements, parameterization

47

48 **1 Introduction**

49 Aerosol hygroscopicity is an important physicochemical property of atmospheric
50 aerosols, representing the extent to which particles take up water when exposed to a certain
51 relative humidity (RH) (Covert et al., 1972). Key parameters describing aerosol hygroscopicity
52 include the scattering enhancement factor, $f(\text{RH})$, which represents the enhancement of the
53 aerosol light-scattering coefficient as a function of RH (Carrico et al., 2003), and κ , the
54 hygroscopicity parameter, whose value is defined by its effect on the water activity of the
55 solution (Petters and Kreidenweis, 2007). Water uptake will increase the size and the mass of
56 hygroscopic aerosols, alter their refractive index, enhance the scattering ability, and ultimately
57 influence the single scattering albedo and aerosol radiative forcing (Cotterell et al., 2017; Titos
58 et al., 2021; Zieger et al., 2013). Furthermore, hygroscopicity affects aerosols' ability to act as
59 CCN (cloud condensation nuclei) and ice nuclei, and further influences cloud properties and
60 precipitation (Cai et al., 2021; Che et al., 2017; Ervens et al., 2007). ~~Climate M~~model results
61 show that even a modest change in κ_{OA} (κ of organic aerosols) can lead to significant changes
62 in CCN, droplet number concentration, and aerosol radiative effects (Liu and Wang, 2010;
63 Rastak et al., 2017). The treatment of aerosol hygroscopicity is one of the key factors
64 contributing to discrepancies between model simulations and observations and among model
65 estimates (Burgos et al., 2020; Haywood et al., 2008; Reddington et al., 2019).

66 Africa emits $\sim 1/3$ of the Earth's annual BB emissions (van der Werf et al., 2010), and
67 its burned areas are increasing every year (Andela et al., 2017). ~~Each~~very Austral spring (July
68 to October), the BB aerosols (BBAs) from African fires are transported westward through the
69 free troposphere (FT) over the persistent stratocumulus cloud deck in the South-East Atlantic
70 (SEA), and eventually subside into the marine boundary layer (MBL) (Redemann et al., 2021).
71 ~~BBAs~~BBA undergo atmospheric processing during transport, altering their chemical
72 composition, oxidation extent, particle polarity, molecular weight, volatility, and solubility

73 (Rastak et al., 2017), making the hygroscopicity highly variable. Laboratory studies show that
74 minutes-old BBA_sBBA are more hygroscopic than hour-old BBA_sBBA (Day et al., 2006),
75 while the hygroscopicity of BBA_sBBA transported for more than several days in the SEA
76 region remains an area of investigation. Furthermore, these BBA_sBBA mix with pristine
77 aerosols and are subject to marine influences from the SEA, resulting in a distinct vertical
78 variation of aerosol hygroscopicity.

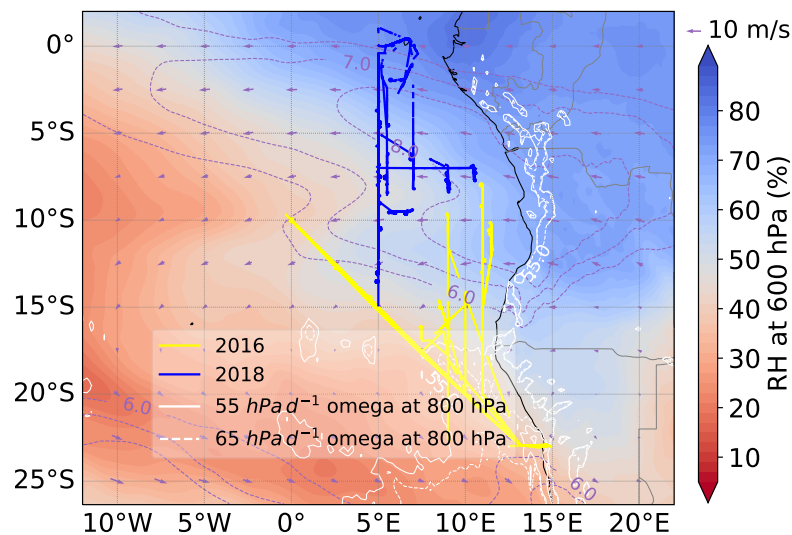
79 The hygroscopicity of organic aerosol (OA), the dominant component of aerosols in
80 most cases, is poorly characterized due to its chemical complexity (Kuang et al., 2020; Mei et
81 al., 2013). Values of κ_{OA} can range from 0 for hydrophobic freshly emitted organics
82 to >approaching 1.0 for very hygroscopic amino acids (Kuang et al., 2020; Petters et al., 2009;
83 Zhang et al., 2007). BBOA is-are usually regarded as hydrophobic, while the mass fraction of
84 aged BBOA shows a positive correlation with κ_{OA} (Cerully et al., 2015; Kuang et al., 2021).
85 Several studies have found a linear correlation between OA hygroscopicity and its oxidation
86 level, commonly characterized by the oxygen-to-carbon (O/C) ratio or the fraction of total
87 organic mass spectral signal at m/z 44 (f_{44}) (Lambe et al., 2011; Mei et al., 2013). However,
88 this linear relationship is not always established, especially for secondary OA with a lower O/C
89 ratio under sub-saturated conditions, for which solubility may play a more important role. In
90 addition, studies show molecular weight, surface tension, and liquid-liquid phase separation
91 are also related to the water affinity of OA (Liu et al., 2018; Rastak et al., 2017; Wang et al.,
92 2019), all contributing to the complexity of OA hygroscopicity.

93 The ORACLES (ObseRvations of Aerosols above CLouds and their intEractionS)
94 campaign (Redemann et al., 2021) provides a comprehensive observation of aerosols above the
95 SEA Ocean with 4-12 days of transport from Africa fires, making it a valuable opportunity to
96 investigate the hygroscopicity of aged BBA and their OA. In this paper, we first characterize
97 the aerosol hygroscopicity and its vertical distribution over the SEA during the BB season, then

98 propose a parameterization relating aerosol hygroscopicity with chemical composition and k_{OA} ,
99 and finally evaluate the sensitivity of aerosol hygroscopicity to k_{OA} . Results are expected to
100 provide a reference to the treatment of aerosol hygroscopicity in climate models and satellite
101 retrievals, and to contribute to aerosol-cloud-interactions and radiative assessments in this
102 climatically important SEA region.

103 2 Methods

104 2.1 Aircraft Instrumentation and Data Analysis



105
106 Figure 1. Flight tracks in 2016 and 2018 ORACLES campaigns. Map of October mean of
107 ERA5 600 hPa RH overlaid by the 600 hPa zonal wind (purple contours; 6, 7, and 8 m s⁻¹),
108 600 hPa horizontal wind vector (purple arrows; m s⁻¹), and ORACLES flight tracks in 2016
109 (yellow) and 2018 (blue), respectively. White contours are the 2016 September mean vertical
110 velocity, omega, at 800 hPa. Solid and dashed lines represent the subsidence of 55 and 65
111 hectopascals per day (hPa d⁻¹).

112 We analyzed airborne, in situ data measured over the SEA region from the ORACLES
113 campaign performed in September 2016 and October 2018 (Redemann et al., 2021). The flight
114 tracks are shown in Fig. 1. All instruments were deployed on the NASA P-3 aircraft. [Aerosol](#)

115 particles were introduced into the P-3 via the solid diffuser inlet. The inlet was operated
116 isokinetically by matching the flow rate to the external air flow velocity to within 5% (Dobracki
117 et al., 2023). This inlet was designed tfor effectively transfer of particles up to 4.0 µm dry
118 diameter (McNaughton et al., 2007). The inner pipework was designed for minimalum
119 transport losses for particles up to 4.0 µm using an online particle loss calculator (Aerosol
120 Calculator, [https://tsi.com/getmedia/540a30fa-8444-49f6-814f-](https://tsi.com/getmedia/540a30fa-8444-49f6-814f-891495c70aa1/Aerocalc2001_1)
121 [891495c70aa1/Aerocalc2001_1](https://tsi.com/getmedia/540a30fa-8444-49f6-814f-891495c70aa1/Aerocalc2001_1)). Two Radiance Research—(RR) M903 integrating
122 nephelometers (Nephs) were operating in parallel, one (referred to as the ‘reference Neph’)
123 under relatively dry conditions and the other (known as the ‘humidified Neph’) maintained at
124 ~80 % RH. ~~Truncation correction has been performed for both Nephs according to Anderson~~
125 ~~and Ogren (1998).~~ Particles entering the reference Neph were heated to the aircraft cabin
126 temperature, significantly reducing their RHs in the Neph and resulting in most particles having
127 an RH below 35%. The humidified Neph was situated downstream of a humidifier, which
128 maintained the RH at the inlet of the Neph at ~80%. ~~A small RH change within the Neph has~~
129 ~~been achieved; more details can be found within a few percent, as detailed in Howell et al.~~
130 ~~(2006). The RH probes in M903 wererhave been corrected based on lab calibrations and the~~
131 ~~Temperature errors are about 0.5°C and RH errors are roughly 3%. The temperature errors are~~
132 ~~about 0.5°C. Measurements were reported at 1 Hz. Particles entering the reference Neph were~~
133 ~~heated to the aircraft cabin temperature, which significantly reduced their RH in the Neph. For~~
134 the calculation of $f(RH)$, data with a reference Neph RH greater than $\geq 30-35\%$ or a humidified
135 Neph RH smaller than $\leq 76\%$ were excluded. The distribution of the RHs of both the reference
136 and humidified Nephs used in this study are shown in Fig. S3X in the supplementary material.
137 Calibrations were performed in the field with refrigerant R-134A (1,1,1,2-tetrafluoroethane).
138 ~~Truncation correction has been~~was performed for both Nephs according to Anderson and

139 [Ogren \(1998\)](#). All scattering coefficients and scattering enhancement factors are reported at
140 540 nm wavelength.

141 The non-refractory submicron aerosol composition was provided by a High-Resolution
142 Time-of-Flight Aerosol Mass Spectrometer (HR-ToF-AMS, Aerodyne Research Inc.) ([Che](#)
143 [Dobracki et al., 2023a](#)). The fragment analysis provided f_{44} and f_{60} , representing the fractions
144 of the OA mass spectrum signals at $m/z=44$ (mainly CO_2^+) and $m/z=60$ (mainly $\text{C}_2\text{H}_4\text{O}_2^+$),
145 respectively, in the total OA mass. The mass concentration of refractory BC was provided by
146 a single particle soot photometer (SP2, Droplet Measurement Technology, [Sedlacek et al.,](#)
147 [2022](#)).

148 The dry particle number size distribution (PNSD) ~~with volume equivalent diameter~~
149 ~~ranging from ~90 nm to 10 μm of PM_{10}~~ was ~~provided by~~ ~~obtained by combining measurements~~
150 ~~from~~ an ultra-high-sensitivity aerosol spectrometer (UHSAS, [Droplet Measurement](#)
151 [Technology](#)) ~~and an aerodynamic particle sizer (APS)~~. ~~The UHSAS was calibrated with~~
152 ~~polystyrene latex (PSL) spheres, whose real refractive index n is 1.572 at the UHSAS laser~~
153 ~~wavelength (Howell et al., 2021)~~. The UHSAS undersized particles ~~in BB plumes; and the~~
154 ~~undersized~~ data were corrected ~~using according to~~ Howell et al. (2021). ~~The PNSD of super-~~
155 ~~micron particles was measured by an aerodynamic particle sizer (APS)~~. The aerodynamic
156 diameter of APS was converted to the volume equivalent diameter according to DeCarlo et al.
157 (2004). Particles were assumed to be spherical (shape factor = 1) with a density of 1.5 g cm^{-3} .
158 ~~However, since the super-micron particles made a minimal contribution to the total scattering~~
159 ~~coefficient, we have neglected the super-micron particles, and only UHSAS measurements are~~
160 ~~used in this study. The minor contribution of super-micron particles to the total scattering~~
161 ~~coefficients is described and illustrated in Section S14 and Fig. S14 in the supplement.~~ -The
162 aerosol/plume age was modelled with a two-week forecast using the Weather Research and
163 Aerosol Aware Microphysics (WRF-AAM) model (Thompson and Eidhammer, 2014). Carbon

164 monoxide was tagged as tracer at the fire source, identified by a burned area product from the
165 moderate resolution imaging spectrometer with a 500 m spatial resolution.

166 All measurements ~~awere~~ averaged to 15 s and adjusted to STP conditions at 273.15 K
167 and 1013 hPa. Data with scattering coefficient $< 10 \text{ Mm}^{-1}$ are not included. ~~$f(\text{RH})$ with $\text{RH} > 30$
168 35% for the reference Neph or $\text{RH} < 76\%$ for humidified Neph are also excluded.~~ The final
169 measurements used in this study have an average RH of $79 \pm 0.5\%$ for the humidified Neph and
170 $\text{RH} < 30\%$ for the reference Neph. To ensure the influence of BB emissions, only data with
171 $f_{60} > 0.003$ are considered (Cubison et al., 2011). This study analyzes measurements from 21
172 flights, totaling approximately 134 flight hours after applying the abovementioned constraints.

173 2.2 Calculation of $f(\text{RH})$ and γ parameterization

174 The aerosol scattering enhancement factor, $f(\text{RH})$, is calculated as:

$$f(\text{RH}) = \frac{\sigma_{sp}(\text{RH})}{\sigma_{sp}(\text{RH}_{ref})} \quad (1)$$

175 where $\sigma_{sp}(\text{RH})$ and $\sigma_{sp}(\text{RH}_{ref})$ represent the scattering coefficients at humidified and reference
176 Neph RHs, respectively. Note the $f(\text{RH})$ only include those with reference Neph RHs equal to
177 or smaller than ~~35~~ 50 % to facilitate comparison with previous studies. For simplicity, we denote
178 the $f(\text{RH})$ at the RH of humidified Neph as $f(80\%)$, despite the small variation of the RH in
179 humidified Neph. The $f(\text{RH})$ is usually fitted to a γ parameterization to apply to a more
180 extensive RH range (Sheridan et al., 2002; Titos et al., 2016):

$$f(\text{RH}) = \left(\frac{1 - \text{RH}/100}{1 - \text{RH}_{ref}/100} \right)^{-\gamma} \quad (2)$$

181 In our case, the γ was calculated with the RH and RH_{ref} using Eq. 2 since the $f(\text{RH})$ was only
182 measured at a fixed RH.

183 2.3 Modeling of $f(\text{RH})$

184 The $f(\text{RH})$ can be modeled with the Mie theory (Mie, 1908). The Python package
185 PyMieScatt (Sumlin et al., 2018), an implementation of the Mie theory (Mie, 1908), was
186 applied in this study. Inputs of PyMieScatt include PNSD and complex refractive index. Dry
187 particles beyond PM_{10} (particulate matter with an aerodynamic diameter less than $1 \mu\text{m}$) are not
188 included in this calculation, supported by their minor contribution to the total scattering, as
189 discussed in Section S1 of the supplement. A volume mixing rule was used to calculate the
190 refractive index. The volume of inorganic salts was converted from those of SO_4^{2-} , NO_3^- , and
191 NH_4^+ from AMS following a modified ion-pairing scheme (Gysel et al., 2007; Zhang et al.,
192 2022). Good agreement has been achieved for calculated and measured scattering coefficients
193 under dry conditions, which indicates good data quality and provides the basis for calculating
194 $f(\text{RH})$ and retrieving $\kappa_{f(\text{RH})}$. The comparison between calculated and measured scattering
195 coefficients is shown in Fig. S4 in the supplement. By combining Mie model with the κ -Köhler
196 theory, we can then calculate the scattering coefficients under humidified RH conditions. For
197 more details of the calculation, refer to Zieger et al. (2013). Subsequently, $f(\text{RH})$ and γ can be
198 obtained using Eq. 1 and 2. The theoretically calculated $f(\text{RH})$ in Sections 3.3.1 and 3.3.2 used
199 an assumed PNSD and different chemical composition combinations. One assumed PNSD was
200 used in these calculations due to its minor impact on $f(\text{RH})$, which has been discussed in detail
201 in Section S2 in the supplement.

202 2.4.3 $\kappa_{f(\text{RH})}$ retrieval and κ_{OA} calculation

203 The aerosol hygroscopicity parameter κ can be retrieved from $f(\text{RH})$, usually denoted
204 as $\kappa_{f(\text{RH})}$ (Chen et al., 2014). It can be regarded as the scattering coefficient weighted average κ
205 (Kuang et al., 2021). ~~The dry scattering coefficient can be computed using Mie theory. The~~
206 ~~Python package PyMieScatt (Sumlin et al., 2018), an implementation of the Mie theory (Mie,~~
207 ~~1908), was applied in this study. Inputs of the Mie model include particle refractive index and~~
208 ~~PNSD. Particles beyond PM_{10} (particulate matter with an aerodynamic diameter less than $1 \mu\text{m}$)~~

209 are not included in this calculation, which can be supported by their small contribution to the
 210 total volume (average < 3 %). By combining Mie model with the κ Köhler theory, we can then
 211 calculate the scattering coefficients under humidified RH conditions. Subsequently, $f(\text{RH})$ and
 212 γ can be obtained using Eq. 1 and 2. In the calculation, a volume mixing rule was used to
 213 calculate the refractive index under both dry and humidified conditions. The volume of
 214 inorganic salts was converted from those of SO_4^{2-} , NO_3^- , and NH_4^+ from AMS following a
 215 modified ion-pairing scheme (Gysel et al., 2007; Zhang et al., 2022). The hygroscopic
 216 parameter κ and density can be found in Table S1. Specifically, we iteratively adjust $\kappa_{f(\text{RH})}$
 217 to minimize the difference between the calculated and measured $f(\text{RH})$. Detailed descriptions
 218 of the retrieval procedure of $\kappa_{f(\text{RH})}$ can be found in Chen et al. (2014).

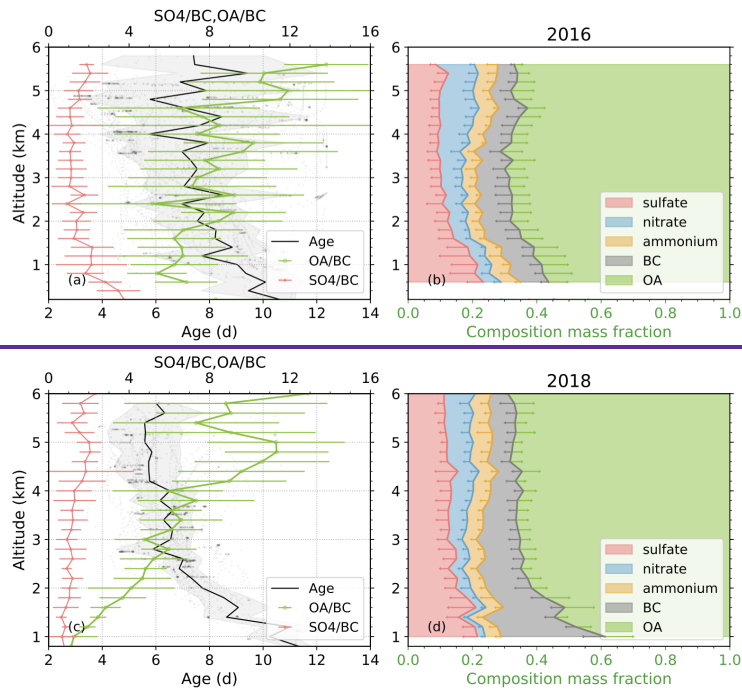
219 According to Petters and Kreidenweis (Petters and Kreidenweis, 2007), the overall
 220 κ_{chem} , which is defined as the κ for the whole aerosol population, can also be calculated from
 221 various chemical compositions following the ZSR (Zdanovskii-Stokes-Robinson) mixing rule.
 222 Kuang et al. (2020b) thoroughly outlined in Section 3.3 that the $\kappa_{f(\text{RH})}$ can accurately represent
 223 the κ_{chem} of $\text{PM}_{1.0}$. Therefore, the hygroscopicity parameter of OA, κ_{OA} , can be calculated as:

$$\kappa_{\text{OA}} = \frac{\kappa_{f(\text{RH})} - (\sum_{i=\text{inorg}} \kappa_i \varepsilon_i + \kappa_{\text{BC}} \varepsilon_{\text{BC}} + \kappa_{\text{OC}} \varepsilon_{\text{OC}})}{\varepsilon_{\text{OA}}}, \quad (3)$$

224 where *inorg* represents inorganic salts, which were derived from the SO_4^{2-} , NO_3^- , and NH_4^+
 225 ions measured from AMS following a modified ion-pairing scheme (Gysel et al., 2007; Zhang
 226 et al., 2022). The subscript *i* denotes each individual inorganic salt. ε represents the volume
 227 fraction of each component, calculated as the ratio of the volume of each component to the
 228 volume of $\text{PM}_{1.0}$. The $\text{PM}_{1.0}$ volume is computed as the sum of the volumes of inorganic salts,
 229 OA, and BC. The hygroscopic parameter κ and density used in this study can be found in Table
 230 S1.

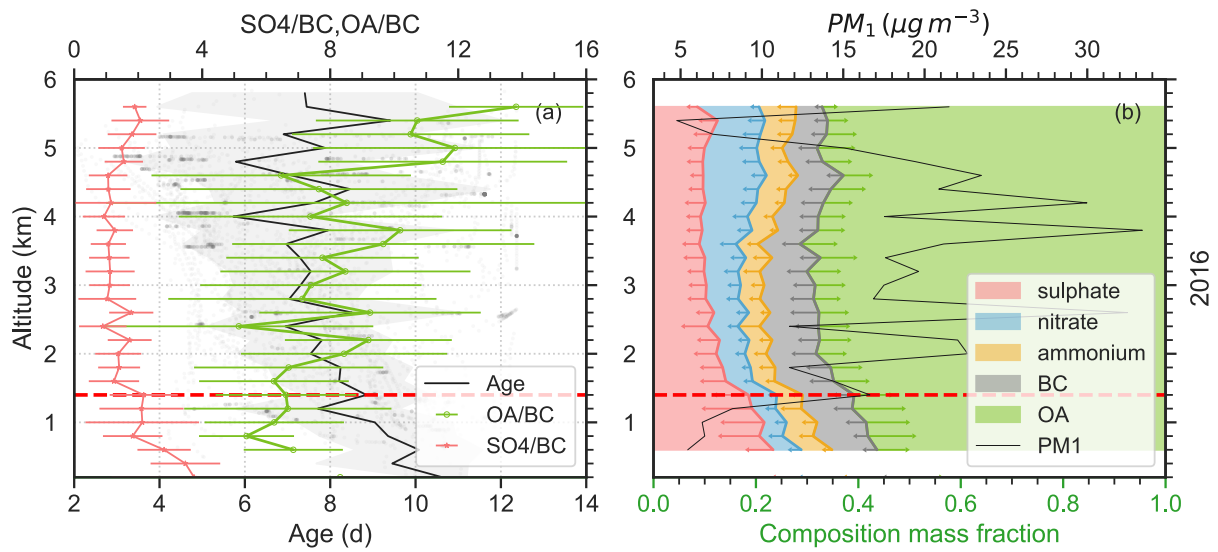
231 3 Results and discussion

3.1 Overview of chemical compositions in 2016 and 2018 ORACLES

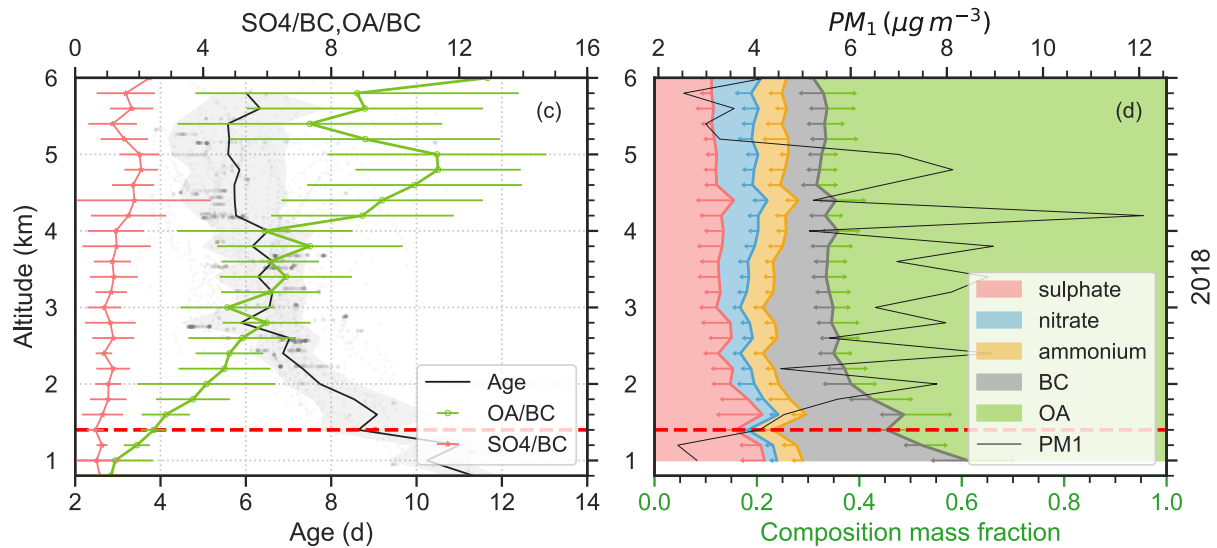


233

234



235



236
 237 Figure 2. The vertical distribution of plume age and chemical composition. (a, c) Variation of
 238 plume age (black), OA/BC, and SO4/BC with altitude in 2016 (upper) and 2018 (lower)
 239 ORACLES campaigns, respectively. Grey dots show the distribution of plume age with the
 240 altitude. (b, d) The average vertical distribution of the mass ratio of chemical compositions and
 241 the average mass concentration of PM₁ from AMS and SP2 in every 200 m in 2016 and 2018
 242 ORACLES campaigns, respectively. The lines are the mean value in every 200 m bin. Errorbars
 243 and grey shading represent the standard deviation in every 200 m bin. The red dashed lines at
 244 1400 m show the maximum height of the MBL during the study period.

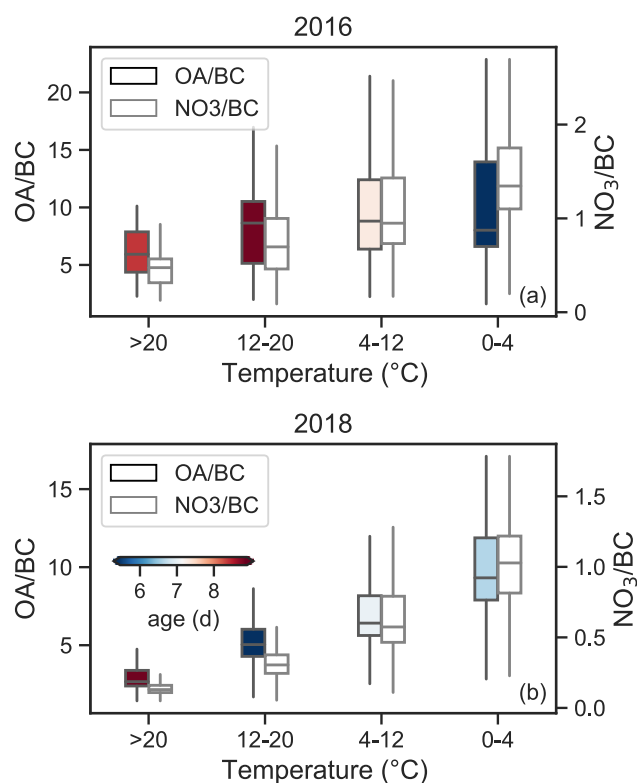
245 Flights in 2016 ORACLES (Fig. 1, yellow lines) are in the region of 8-24° S and 0-15°
 246 E, traversing both the southern African Easterly Jet (AEJ-S) region and the continent
 247 anticyclone (Ryoo et al., 2021). As a result, aerosols around 600–700 hPa3-4 km in 2016
 248 ORACLES include both less aged (<4 d) particles coming directly from the continent and
 249 highly aged (>10 d) particles transported from the west/north, resulting in a larger variation of
 250 plume age in each level as shown in Fig. 2a. At lower altitudes, aerosols are less aged than
 251 those in the 2018 campaign due to the subsidence (positive values of omega) near the Namibian
 252 coast (Fig. 1a). During the 2016 campaign, the cloud top is generally below 1.5 km. The 2018
 253 ORACLES flights, represented by blue lines in Fig. 1, are primarily situated within the 0-15°

254 S and 5-10° E coordinates. The cloud top in this region is a bit lower than in 2016 campaign,
255 centering around 1 km. This area generally coincides with the region influenced by the southern
256 African Easterly Jet (AEJ-S). ~~BB A aerosols~~ are lifted up to the free troposphere, transported
257 westward by AEJ-S and then subside into the marine boundary layer, rendering the distinct
258 vertical age pattern that increases with the decreasing altitude (Fig. 2c). Correspondingly,
259 aerosols in the SEA region during BB season exhibit distinct vertical distribution of chemical
260 composition. From Fig. 2b and 2d, the vertical profiles of chemical composition fractions are
261 generally consistent during 2016 and 2018 ORACLES campaigns. In this section, we focused
262 on the variation of OA and sulphate, two components that dominate aerosol hygroscopicity in
263 the SEA.

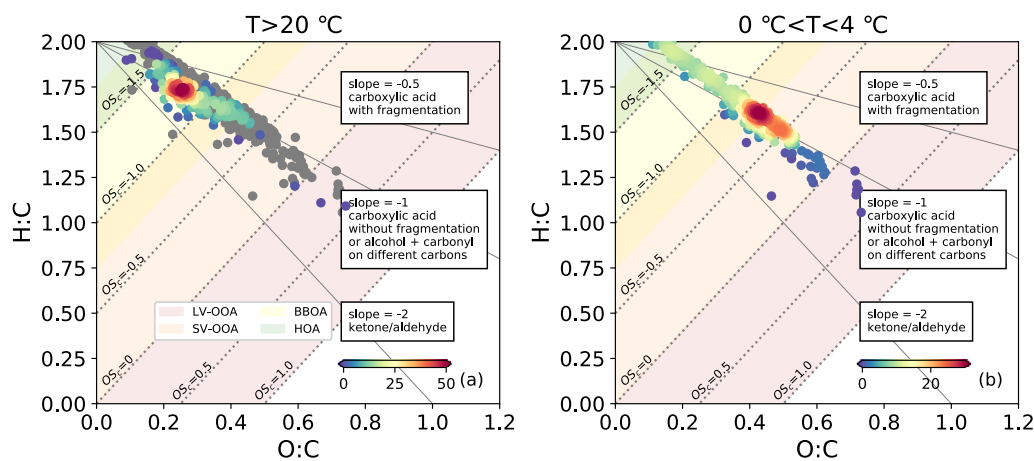
264 OA constitutes the largest fraction of aerosol mass in ORACLES, approximately 60 %.
265 The OA mass fraction in both years shows little variation above 2 km; below this altitude, OA
266 mass fraction decreases with decreasing altitude, in contrast to the trend of the sulphate mass
267 fraction. The OA/BC ratio, representing the OA mass concentration normalised by that of BC
268 to remove the dilution effect during transport and an indication of OA processing, differs in
269 2016 and 2018. While 2018 data shows a clear decrease in OA/BC with decreasing altitude,
270 the decrease was less pronounced in 2016, showing considerable variation at identical altitudes.
271 In the meanwhile, the OA/BC shows a clear reverse trend with the plume age in 2018, this
272 inverse relationship is less obvious in 2016. Dobracki et al. (2022) used RH as an indicator to
273 investigate the importance of thermodynamic partitioning in OA/BC changes during the 2016
274 ORACLES campaign, concluding that it accounts for no more than 10 % of the changes. The
275 dominant factor is believed to be the oxidation of OA through fragmentation. A similar result
276 is found in this study using temperature as an indicator, as shown in Fig. 3a. Please note Fig. 3
277 only considers OA above 1.4 km and temperature > 0 °C to minimize the marine influence and
278 to exclude possible ice nucleation. The OA/BC ratio in the 2016 ORACLES campaign did not

279 show a clear decrease with increasing temperature, as NO_3/BC did, which is a result of
280 thermodynamic repartition to the gas phase. However, in the 2018 ORACLES campaign, we
281 did notice a significant decrease of OA/BC with increasing temperature (Fig. 3b). The OA/BC
282 decreased $\sim 70\%$ from 9.7 ± 3.1 for temperature $0\text{--}4\text{ }^\circ\text{C}$ to 2.9 ± 0.9 for temperature $> 20\text{ }^\circ\text{C}$, only
283 slightly lower than the decrease of NO_3/BC , $\sim 85\%$. Yet, we cannot simply attribute the OA/BC
284 changes to thermodynamic repartition while disregarding the effect of ageing or OA oxidation.
285 In 2018, temperature and plume age are closely correlated (Pearson correlation coefficient of
286 0.51), and the decrease in OA/BC is accompanied by ageing (Pearson correlation coefficient
287 of 0.57), as shown in Fig. 2a and b. We utilized the oxidation state to differentiate between the
288 effects of thermodynamic repartition and OA oxidation. Figure 4 shows the Van Krevelen
289 diagrams (H/C vs. O/C, Ng et al., 2011) for aerosols ~~under-at~~ temperatures $> 20\text{ }^\circ\text{C}$ and $0\text{--}4\text{ }^\circ\text{C}$.
290 The estimated carbon oxidation state (OS_C), defined as $\text{OS}_\text{C} = 2\text{O}/\text{C} - \text{H}/\text{C}$, can also indicate
291 different OA volatility regimes, with OS_C of $-2.0\text{--}-1.5$ for HOA (hydrocarbon-like OA), $-$
292 $1.75\text{--}-0.75$ for BBOA (biomass burning OA), $-1.0\text{--}0.0$ for SV-OOA (semi-volatile oxidized
293 OA), and $0.0\text{--}1.0$ for LV-OOA (low volatility oxidized OA) (Donahue et al., 2012; Kroll et
294 al., 2011). If thermodynamic repartition plays a more crucial role, the OA remaining under
295 higher temperature would be less volatile due to evaporation of more volatile OA. Notably, we
296 found the opposite. From Fig. 4, aerosols ~~under-at~~ temperature $> 20\text{ }^\circ\text{C}$ (lower altitudes) are
297 generally more volatile than those at temperature $0\text{--}4\text{ }^\circ\text{C}$ (higher altitudes). This indicates that
298 thermodynamic repartition is not a dominant factor in OA/BC changes, and that the OA
299 oxidation through fragmentation is more important in OA/BC changes in 2018, consistent with
300 the 2016 campaign as well as results in Dobracki et al. (2022). This is also in line with the
301 findings of Dang et al. (2022) which found less organics in aerosols collected on filters
302 associated with more aged plumes and more rounded and viscous organics on filters sampled
303 from less aged plumes. For OA below 1.4 km, aqueous phase reactions and cloud scavenging

304 might also contribute to the loss of OA during the entrainment and within the MBL (Che et al.,
 305 2021; Wu et al., 2020).



306
 307 Figure 3. OA/BC (black outline) and NO₃/BC (grey outline) mass ratios as a function of
 308 ambient temperature in 2016 (a) and 2018 (b) ORACLES campaign, for altitude > 1.4 km and
 309 temperature > 0 °C. The boxes represent the 10th percentile, 25th percentile, median, 75th
 310 percentile, and 90th percentile.



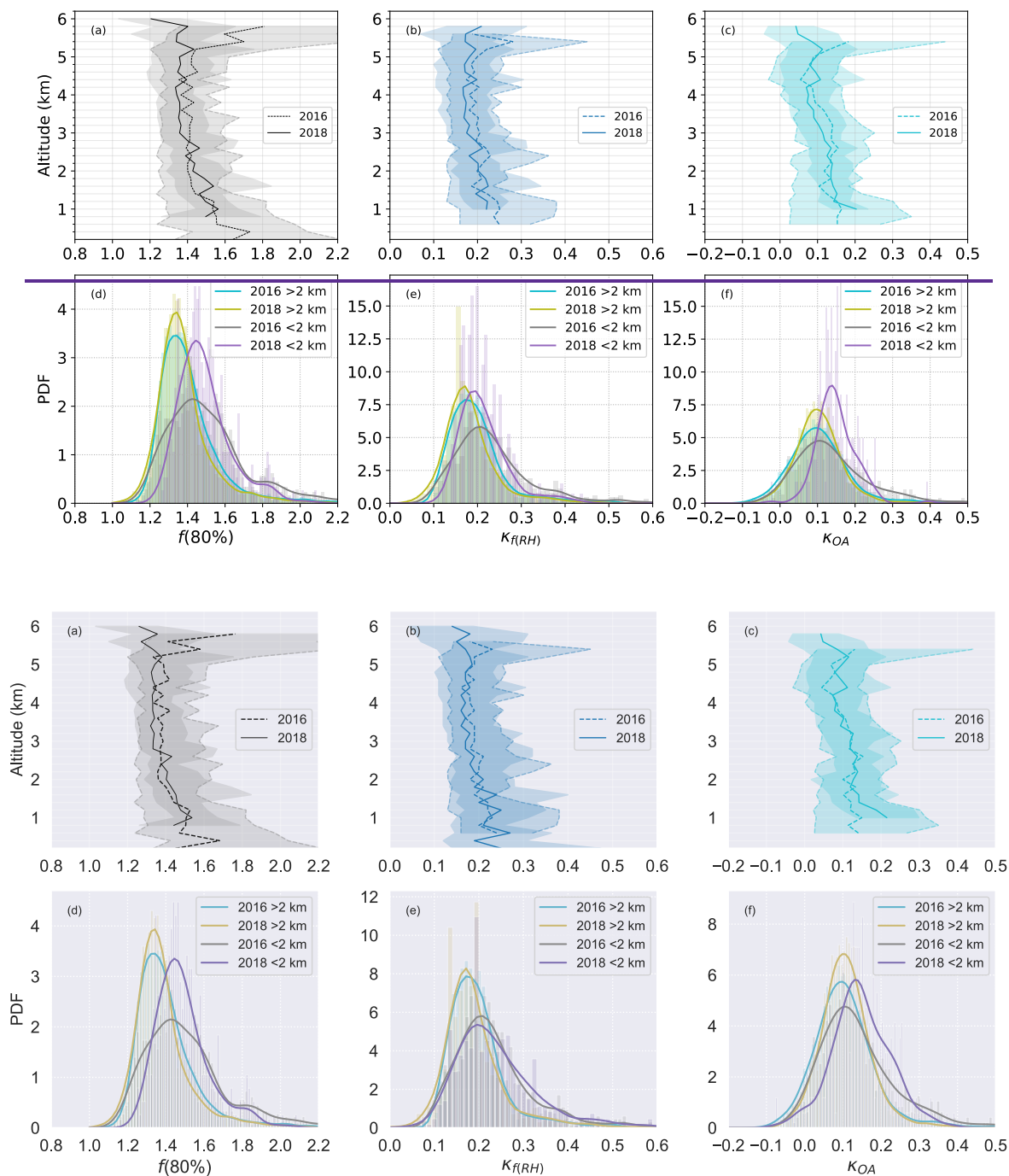
312 Figure 4. Van Krevelen diagram (H/C vs. O/C) for aerosols with temperature higher than 20 °C
313 (a) and with temperature lower than 4 °C (b). The color scale indicates the density of the data
314 in each plot. The grey dots in (a) are the Van Krevelen diagram of aerosols with temperature
315 lower than 4 °C, the same as (b).

316 The variation of sulphate mass fraction remains largely constant above 2 km, and below
317 2 km, increases with decreasing altitudes. The higher sulphate fraction at lower altitudes is
318 consistent with the observations from CLARIFY-2017 (CLOUD-Aerosol-Radiation Interaction
319 and Forcing for Year 2017) campaign (Wu et al., 2020), which was conducted downwind of
320 ORACLES in the SEA ocean. This higher sulphate fraction at lower altitudes results from the
321 increase of SO₄/BC and decrease of OA/BC. SO₄/BC ratio generally remains constant above
322 800 m in both years' campaign. However, for 2016 ORACLES campaign, where there are
323 samples below 800 m, the ratio shows an increase with decreasing altitude. This increase could
324 indicate a sulphate contribution from the ocean, either in the form of sea-salt sulphate or
325 through [the oxidation of](#) dimethylsulfide (DMS) emitted by marine phytoplankton. The latter
326 can contribute to non-sea-salt sulphate by oxidizing to SO₂ and further to sulphate (Mayer et
327 al., 2020; Alexander et al., 2005). Notably, part of the 2016 flight region, especially the SEA
328 offshore of Namibia, is known as an upwelling region with high DMS emissions (Andreae et
329 al., 1995). Klopper et al. (2020) have attributed 57 % of sulphate to sea salt and 43 % to non-
330 sea-salt sulphate along the Namibian coast. These findings align with model simulations
331 showing that DMS is the third largest CCN source in the SEA up to 2 km (Che et al., 2022b).

332 Furthermore, BC mass constitutes approximately 10 % of the PM₁ mass fraction,
333 indicating the large influence of BB in this region. The nitrate mass fraction increases with
334 increasing altitude in all layers, which is consistent with the findings of CLARIFY, and can be
335 explained by the shift of gas-particle partitioning of the HNO₃-NH₃-NH₄NO₃ system towards
336 the aerosol phase at the lower temperatures found at higher altitudes (Wu et al., 2020). The

337 mass fraction of ammonium stays stable with height, approximately 5 %. We neglected
 338 chloride in this study as it accounts for less than 1±1% mass fraction.

339 3.2 Aerosol hygroscopicity in SEA in 2016 and 2018 ORACLES



340
 341
 342 Figure 5. Vertical profiles and PDF of $f(80\%)$ (a, d), $\kappa_{f(RH)}$ (b, e), and κ_{OA} (c, f) for aerosols in
 343 the 2016 (dotted line) and 2018 (solid line) ORACLES campaign. Dashed linesThe lines in a,

b, and c represent the medians, and the shadings in a, b, and c represent the 10th percentile, mean, and 90th percentile, respectively.

In general, the aerosol hygroscopicity stays stable above 2 km in both years' campaigns; while below 2 km, aerosols become more hygroscopic at lower altitudes (Fig. 5). The results from the Levene's test for medians for $f(80\%)$, $\kappa_{f(RH)}$, and κ_{OA} indicate that $f(80\%)$, $\kappa_{f(RH)}$, and κ_{OA} are statistically different above and below 2 km, with a confidence level of 95%. This is consistent with the vertical variation of sulphate and OA mass fraction, i.e. more sulphate and less OA at lower altitudes (Fig. S5). The probability density function (PDF) distributions of $f(80\%)$ and $\kappa_{f(RH)}$ are similar in the 2016 and 2018 campaigns, with larger variations and higher values of the aerosol hygroscopicity PDF under 2 km (Fig. 5d and 5e). For $f(80\%)$ below 2 km, a primary mode with a diameter value of around 1.45 is evident, but there is also a second mode with a diameter value of around 1.81 for aerosols in both years. While the second mode is subtle, it can be identified in the PDF of $\kappa_{f(RH)}$ (Fig. 5e). This suggests the presence of highly hygroscopic substances and could indicate marine influence, as most aerosols below 2 km are within the MBL. For aerosols above 2 km, the mean and standard deviation of $f(80\%)$ and $\kappa_{f(RH)}$ are 1.40 ± 0.17 and 0.19 ± 0.07 , respectively (Fig. 5, Table 1, and Table S2). These values indicate less hygroscopic particles (Liu et al., 2011) and are lower than those for marine aerosols (Zieger et al., 2010; Carrico et al., 2003) but higher than those for dust and polluted dust particles (Bukowiecki et al., 2016; Zhang et al., 2015a). They are comparable to smoke-dominated aerosols, such as the smoke from savanna fires in Australia (Gras et al., 1999) and the BBAs from forest fires in the northeast US (Wang et al., 2007). These values are slightly higher than the $f(80\%)$ in Brazil (SCAR-B) (Kotchenruther and Hobbs, 1998). The particles below 2 km are more hygroscopic (Liu et al., 2011). The mean and standard deviation of $f(80\%)$ and $\kappa_{f(RH)}$ are 1.51 ± 0.22 and 0.23 ± 0.08 , respectively, placing them in the upper ranges of BBA hygroscopicity reported in the literature. These values are comparable to those

369 of the aged smoke in Africa (SAFARI, Magi and Hobbs, 2003) and the Yangtze River Delta
370 background station (Zhang et al., 2015a). They match the $\kappa_{(RH)}$ of 0.22 at a rural site in southern
371 China (Kuang et al., 2021) but are lower than the values for BBAs in East Asia (ACE-
372 Asia, Kim et al., 2006) and agricultural burning in INDOEX (Indian Ocean Experiment,
373 Sheridan et al., 2002). For aerosols above 2 km, the mean and standard deviation of $f(80\%)$ and
374 $\kappa_{(RH)}$ are 1.40 ± 0.17 and 0.19 ± 0.07 (Fig. 5 and Table S2), respectively, belonging to less
375 hygroscopic particles (Liu et al., 2011). These values are generally lower than those for marine
376 aerosols (Zieger et al., 2010; Carrico et al., 2003), higher than dust and polluted dust particles
377 (Bukowiecki et al., 2016; Zhang et al., 2015a), and consistent with the median level of the
378 hygroscopicity for smoke-dominated aerosols found in the literature. They are comparable to
379 the $f(80\%)$ of 1.37 for smoke from lightly wooded savanna fires in Australia ($D_p < 3 \mu\text{m}$) (Gras
380 et al., 1999), and the $f(82\%)$ of 1.40 for BBAs from forest fires in northeast US (Wang et al.,
381 2007); while slightly higher than the $f(80\%)$ of BBAs in Brazil (SCAR-B, $D_p < 4 \mu\text{m}$)
382 (Kotchenruther and Hobbs, 1998). For aerosols below 2 km, they belong to more hygroscopic
383 particles (Liu et al., 2011). The mean and standard deviation of $f(80\%)$ and $\kappa_{(RH)}$ are 1.51 ± 0.22
384 and 0.23 ± 0.08 , respectively, which belong to the upper ranges of BBA hygroscopicity in the
385 literature. These values are comparable to the $f(80\%)$ of 1.42 ± 0.05 for smoke collected between
386 10 and 50 min of emission in Africa (SAFARI, $D_p < 5 \mu\text{m}$) (Magi and Hobbs, 2003), the $f(80\%)$
387 of 1.43 ± 0.12 in a background station in the Yangtze River Delta of China (Zhang et al., 2015a),
388 and the $\kappa_{(RH)}$ of 0.22 ± 0.04 in a rural site in southern China (Kuang et al., 2021); while lower
389 than the $f(85\%)$ of 1.60 ± 0.20 for BBAs in East Asia during ACE-Asia (Asian Pacific regional
390 aerosol characterization experiment) (Kim et al., 2006), the $f(85\%)$ of 1.58 ± 0.21 for
391 agricultural burning in INDOEX (Indian Ocean Experiment) (Sheridan et al., 2002), the $f(80\%)$
392 of 1.66 ± 0.08 for fresh smoke (within 10 min from emission) in Africa (Magi and Hobbs, 2003).
393 Comparing to the κ obtained from CCN measurements at a similar location in August 2017

394 ORACLES (Kacarab et al., 2020), our results are ~ 30 % lower. This difference is expected
 395 because κ values obtained under supersaturated conditions are typically larger than those from
 396 sub-saturated conditions (Petters and Kreidenweis, 2007). This highlights the significance of
 397 using the appropriate κ for sub-saturated and supersaturated investigations, such as when
 398 examining aerosol liquid water content and cloud condensation nuclei activation (Rastak et al.,
 399 2017; Petters and Kreidenweis, 2007).

400 [Table 1. The \$f\(RH\)\$ of biomass burning aerosol from the literature.](#)

f(RH)	RH	Location	Fuel type and notes	Reference
1.37	80%	Australia	light-wooded savanna fires	Gras et al., 1999
1.40	82%	northeast US	forest fires	Wang et al., 2007
1.16	80%	Brazil (SCAR-B^a)	grass, shrub, and trees	Kotchenruther and Hobbs, 1998
1.44 ± 0.02	80%	Southern Africa (SAFARI 2000^b)	aged heavy smoke	Magi and Hobbs, 2003
1.60±0.20	85%	Korea (ACE-Asia^c)	BBA	Kim et al., 2006
1.58±0.21	85%	India Ocean (INDOEX^d)	agricultural burning	Sheridan et al., 2002
1.51±0.22	80%	South-East Atlantic Ocean (below 2 km, ORACLES)	savanna^e	This study
1.40±0.17	80%	South-East Atlantic Ocean (above 2 km, ORACLES)	savanna^e	This study

401

402 [^a Smoke, Clouds, and Radiation-Brazil](#)

403 [^b Southern African Regional Science Initiative 2000](#)

404 [^c Aerosol Characterization Experiment](#)

405 [^d Indian Ocean Experiment](#)

406 [^e Che et al., 2022](#)

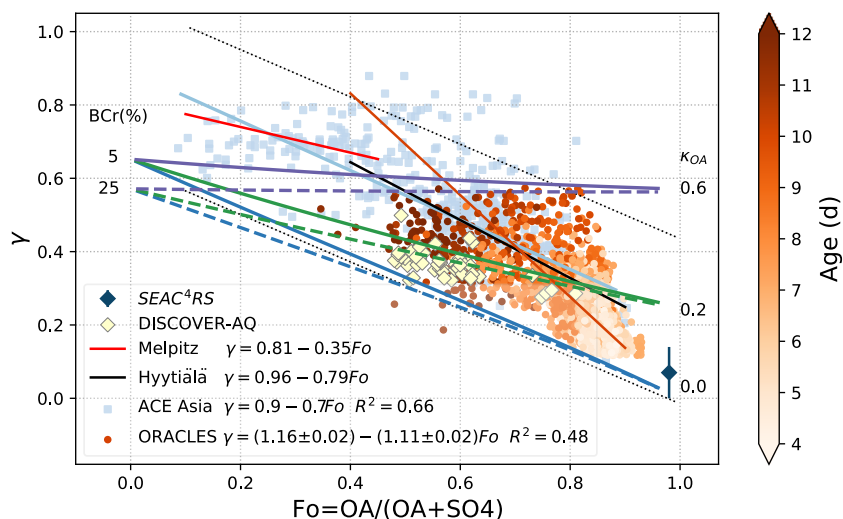
407 The mean κ_{OA} (± 1 standard deviation) is 0.11 ± 0.08 , with the 25th and 75th percentiles
 408 of 0.06 and 0.16. From the vertical profiles, more hygroscopic OA are generally more aged,
 409 highly oxidized, and usually located at lower altitudes (Fig. 2 and 5). In addition, we observed
 410 a slight increase in κ_{OA} with volatility in 2016, with a Pearson correlation coefficient of -0.35

411 between κ_{OA} and OSc, contrasting the conventional understanding that the most volatile
412 compounds have the least hygroscopicity. This trend has been observed, albeit rarely, in field
413 and laboratory studies (e.g. Cerully et al., 2015; AsaAwuku et al., 2009). It may be related to
414 fragmentation during OA oxidation, where the highly aged and low volatile OA may dissociate
415 into more volatile fragments that are still highly functionalized and hygroscopic. However, in
416 general, no clear correlation has been found between κ_{OA} with altitude or oxidation level.

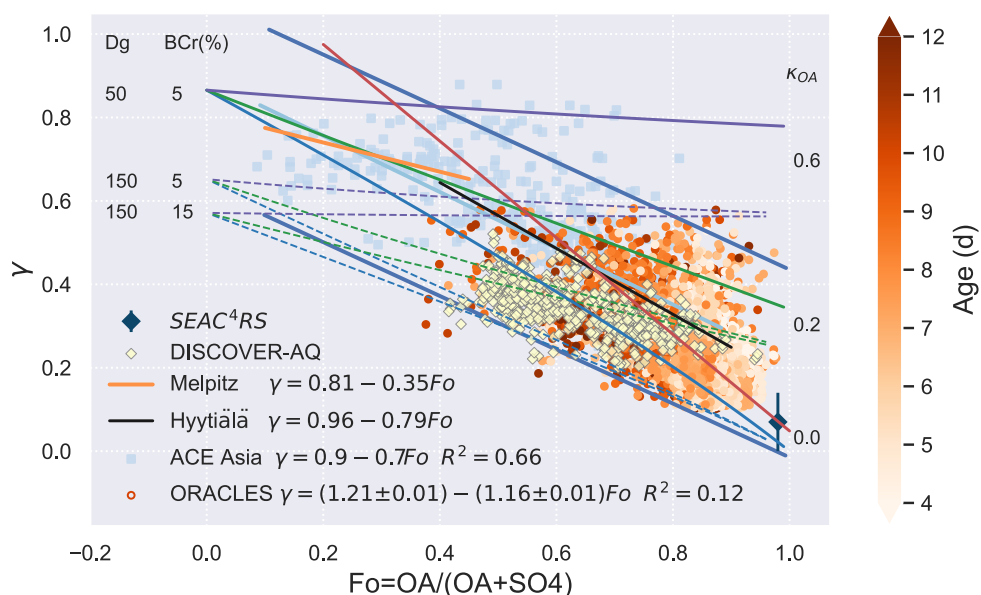
417 We noted a portion of highly aged aerosols (> 10 d) in 2016 having high OA/BC (> 12 ,
418 corresponding OA mass fraction > 50 %), in contrast to the general trend that more aged
419 aerosols correspond to smaller OA/BC (Fig. 2). About 95 % of these aerosols are above 3 km
420 and have a slightly lower f_{44} than the campaign average (Fig. S1aS6a). Approximately 60 %
421 belong to LV-OOA with OSc > 0 and 40 % are SV-OOA (Fig. S1bS6b). As shown in Fig.
422 S1eS6c, the κ_{OA} values are smaller for these aerosols compared to the whole 2016 campaign,
423 which is consistent with previous studies that κ_{OA} is lower for less oxidized OA (Kuang et al.,
424 2020; Rastak et al., 2017; Mei et al., 2013); though we do not observe such correlation for the
425 entire campaign. We hypothesize that thermodynamic^{al} repartitioning has played a role, i.e.
426 less-oxidized materials condensed onto pre-existing OA under low temperature at high
427 altitudes, resulting in smaller f_{44} values and contributing to SV-OOA. These less-oxidized
428 materials are generally less functionalized and less hygroscopic, which would lead to a lower
429 κ_{OA} .

430 3.3 Relationship with chemical composition and κ_{OA}

431 3.3.1 Comparison with various campaigns



432



433

434 Figure 6. γ versus F_o in various campaigns and for internally mixed $\text{OA}-(\text{NH}_4)_2\text{SO}_4$ -BC
 435 mixtures. F_o represents the ratio of mass concentrations of OA to OA and SO_4^{2-} . Solid lines in
 436 light blue and brown-red represent the linear fits for ACE-Asia and ORACLES, respectively.
 437 Dotted grey/Solid blue lines show the 95% prediction bands for the ACE-Asia data, in light
 438 blue rectangles, taken from Quinn et al. (2005). Colorbar represents the plume age (days) in
 439 ORACLES. Data for SEAC⁴RS is shown by dark blue diamond, taken from Shingler et al.
 440 (2016). DISCOVER-AQ data is shown by yellow diamonds, taken from NASA Langley

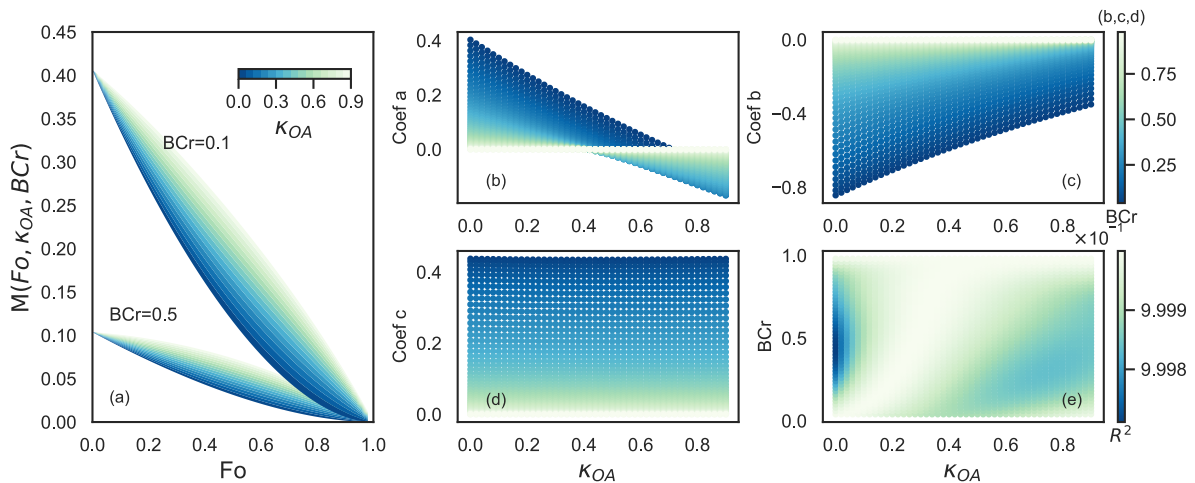
441 Research Center Atmospheric Science Data Center (Atmospheric Science Data Center, 2015).
442 Fitting lines for two European sites Melpitz (solid ~~red-orange~~ line) and Hyytiälä (solid black
443 line) are from Zieger et al. (2015). Blue, green, and purple lines represent results for internally
444 mixed OA-(NH₄)₂SO₄-BC mixtures with 1) a range of BC mass fraction (BCr, solid for 5%
445 and dashed for 25%) and 2) OA with κ_{OA} of 0 (blue), 0.2 (green), and 0.6 (purple) from Mie
446 calculations assuming a lognormal size distribution with a geometric mean diameter D_{gn} of 150
447 nm and a standard deviation σ_{sg} of 1.65.

448 Quinn et al. (2005) proposed a parameterization quantifying the relationship between γ
449 and F_o , the ratio of mass concentrations of OA to OA and SO_4^{2-} , based on measurements in
450 ACE-Asia. We applied the parameterization to ORACLES measurements and as shown in Fig.
451 6, our data are well within the 95% prediction confidence intervals. We further investigated the
452 γ - F_o dependence of ~~BBA~~BBA from DISCOVER-AQ and SEAC⁴RS (Shingler et al., 2016)
453 and continental aerosols from the central European station Melpitz and a boreal site Hyytiälä
454 in Finland (Zieger et al., 2014, 2015), all showed good overlap with those from ACE-Asia and
455 ORACLES. The linear regression for ORACLES, $\gamma = (1.16 \pm 0.02) - (1.11 \pm 0.02)F_o$, retrieved
456 from an orthogonal fit by taking the standard deviation as the input for uncertainty calculation,
457 is very similar to those in Hyytiälä and ACE-Asia, though the slope is slightly lower.

458 We explored the γ - F_o relationship with the Mie model and found that the relationship
459 observed can be largely explained by aerosol chemical composition and OA hygroscopicity.
460 The γ values were calculated with the scattering coefficients simulated at both dry conditions
461 and 80 % RH were performed with Mie model for internally mixed OA-(NH₄)₂SO₄-BC
462 mixtures with assumed BC mass ratio (BCr, 5 % and 25 %), and κ_{OA} values (0-0.6), which
463 encompass the ranges observed in ORACLES (refer to Sect. 3.2 for κ_{OA} values). The PNSD
464 was ~~calculated following assumed to being it was~~ the lognormally distributed ion, with the
465 geometric mean diameter (D_{gn}) of 150 nm and the standard deviation (σ_{sg}) of 1.6~~with the~~

466 geometric mean diameter (D_{gn}) and standard deviation (σ_{sg}) set to $D_{gn}=150$ nm and $\sigma_{sg}=1.6$,
 467 respectively. As shown in Fig. 6 (solid and dashed purple, green, and blue lines), simulated
 468 curves can capture most of the observations. Fo and κ_{OA} dominant γ , and BC shows a small
 469 negative impact. It is noteworthy that the (negative) slope of the γ -Fo relationship increases
 470 with increasing κ_{OA} up to κ_{OA} values of 0.6, where γ exhibits little variation with Fo. Therefore,
 471 we conclude that the variation of BBA hygroscopicity with ageing in the SEA is mainly due to
 472 changes in chemical composition, particularly sulphate and OA, as well as the variation of OA
 473 hygroscopicity during transport. The higher BC fraction in aged aerosols compared to less aged
 474 ones has slightly decreased the hygroscopicity of aged aerosols.

475 3.3.2 Parameterization of γ using Mie simulations of internally mixed OA-(NH₄)₂SO₄- 476 BC mixtures



477
 478 Figure 7. (a) Variations of $M(Fo, \kappa_{OA}, BCr)$ with Fo coloured by κ_{OA} at BCr of 0.1 and 0.5,
 479 respectively, for internally mixed OA-(NH₄)₂SO₄-BC mixtures. $M(Fo, \kappa_{OA}, BCr)$ is the product
 480 of $\gamma(Fo, \kappa_{OA}=0, BCr)$ and $\gamma(Fo, \kappa_{OA}, BCr)$ for each κ_{OA} value. Fo represents the ratio of the mass
 481 concentration of OA to that of OA and SO_4^{2-} . BCr is the mass ratio of BC. (b,c,d) Variation of
 482 coefficients a, b, and c with κ_{OA} and BCr . The coefficients a, b, and c are the fitted parameters
 483 of the quadratic regression between $M(Fo, \kappa_{OA}, BCr)$ and Fo for each κ_{OA} and BCr . (e) The R^2
 484 (colorbar) of the $M(Fo, \kappa_{OA}, BCr)$ regression with Fo as a function of κ_{OA} and BCr .

485 Mie simulations are performed for internally mixed OA-(NH₄)₂SO₄-BC mixtures to
 486 obtain the scattering coefficient of dry and humidified aerosols. We assume PNSD to be a log-
 487 normal distribution with D_{gn}=150 nm and σ_{sg} = 1.6, as the approximation of the D_{gn} and σ_{sg} in
 488 ORACLES 2016 and 2018 campaigns. The RH and RH_{ref} is set as 80 % and 0, respectively.
 489 The γ is then calculated following Eq. 2. The Fo, κ_{OA}, and BCr are varied from 0 to 1, 0 to 0.9,
 490 and 0 to 1, respectively, all ~~in increments with a span~~ of 0.02. Taking γ(Fo,κ_{OA}=0,BCr) as the
 491 baseline (refer to solid and dashed blue lines in Fig. 6), we calculated the product
 492 M(Fo,κ_{OA},BCr) of γ(Fo,κ_{OA}=0,BCr) and γ(Fo,κ_{OA},BCr) for each κ_{OA} and BCr, i.e.
 493 M(Fo,κ_{OA},BCr)= γ(Fo,κ_{OA}=0,BCr)* γ(Fo,κ_{OA},BCr), and found that the relationship between
 494 M(Fo,κ_{OA},BCr) and Fo can be well fitted into a quadratic (second-order) polynomial function,
 495 i.e. M(Fo,κ_{OA},BCr) = aFo²+bFo+c (Fig. 7a). The variation of M(Fo,κ_{OA},BCr) with Fo and the
 496 R² of the regression are shown in Fig. 7a and 7e, respectively. The fitted coefficients a, b, and
 497 c, as shown in Fig. 7b, 7c, and 7d, coincidentally fit well as quadratic functions of κ_{OA}, whose
 498 coefficients, in turn, can be well fitted into a fifth-order polynomial function of BCr. Results
 499 are shown in Fig. S3 in the supplement. In sum, the M(Fo,κ_{OA},BCr) can be parameterized as:

$$M(F_o, \kappa_{OA}, BCr) = \sum_{\substack{i \leq 2 \\ j \leq 2 \\ k \leq 5}} a_{ijk} BCr^k \kappa_{OA}^j F_o^i \quad (4)$$

500 Similarly, γ(Fo,κ_{OA}=0,BCr) can be well fitted into a quadratic function of Fo with coefficients
 501 that fit well with a fifth-order polynomial function of BCr:

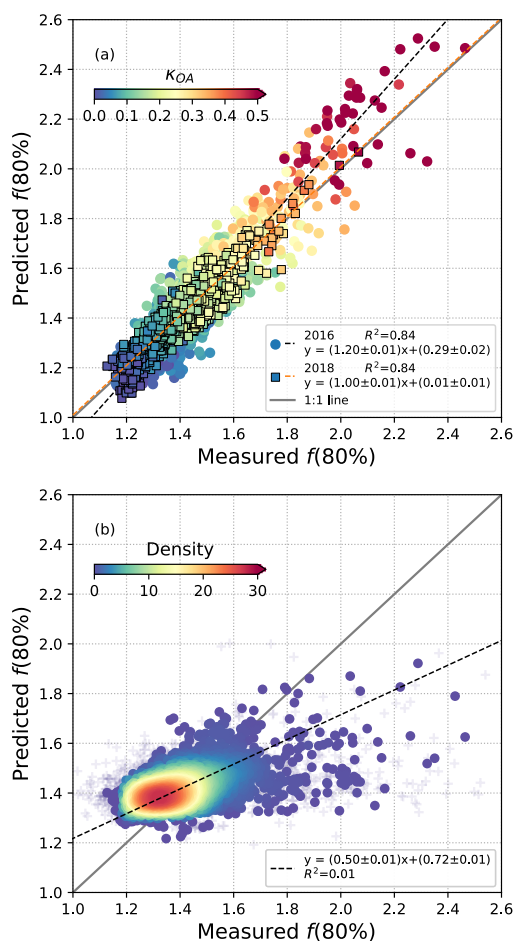
$$\gamma(F_o, \kappa_{OA} = 0, BCr) = \sum_{\substack{i \leq 2 \\ k \leq 5}} a_{ik} BCr^k F_o^i \quad (5)$$

502 Equations 4 and 5 in matrix format are referred to Eq. S1 and S2 in the supplement,
 503 respectively. Values of coefficients a_{ijk} and a_{ik} are shown in Table S3. Therefore,
 504 γ(Fo,κ_{OA},BCr) can be calculated as the ratio of M(Fo,κ_{OA},BCr) to γ(Fo,κ_{OA}=0,BCr):

(6)

$$\gamma(F_o, \kappa_{OA}, BCr) = M(F_o, \kappa_{OA}, BCr) / \gamma(F_o, \kappa_{OA} = 0, BCr)$$

505 The $f(\text{RH})$ can then be calculated with Eq. 2. We evaluated this parameterization by comparing
 506 the predicted and measured $f(80\%)$ in ORACLES 2016 and 2018 campaigns. The predicted
 507 $f(80\%)$ is calculated with Eq. 6 with F_o , κ_{OA} , and BCr as inputs and Eq. 2 with the dry and
 508 humidified RHs measured in both campaigns. Note the mean BC mass ratio for each year has
 509 been used in the calculation, as little difference has been observed using the temporal BCr and
 510 mean BCr . Good correlation of measured and predicted $f(80\%)$ has been achieved for both
 511 years' campaign, as shown in Fig. 8a. This indicates that the internally mixed $\text{OA}-(\text{NH}_4)_2\text{SO}_4$ -
 512 BC mixture with PNSD ($D_{\text{gn}}=150$ nm and $\sigma_{\text{sg}} = 1.6$) is a good approximation of aerosols with
 513 respect to the $f(\text{RH})$ prediction in 2016 and 2018 ORACLES campaign. The influence of PNSD
 514 on $f(\text{RH})$ is small and discussed in Section S1 in the supplement.



515

516 Figure 8. Measured $f(80\%)$ vs predicted $f(80\%)$ using the γ parameterization for internally
517 mixed OA-(NH₄)₂SO₄-BC mixtures. The $f(80\%)$ in subplot (a) is calculated with κ_{OA} values
518 coloured by κ_{OA} , and in subplot (b) is predicted with the mean κ_{OA} values. Black and orange
519 dashed lines in subplot (a) represent the ordinary linear regression for 2016 and 2018,
520 respectively. The black dashed line in subplot (b) represents the ordinary linear regression for
521 the two years. Grey solid line is the 1:1 line.

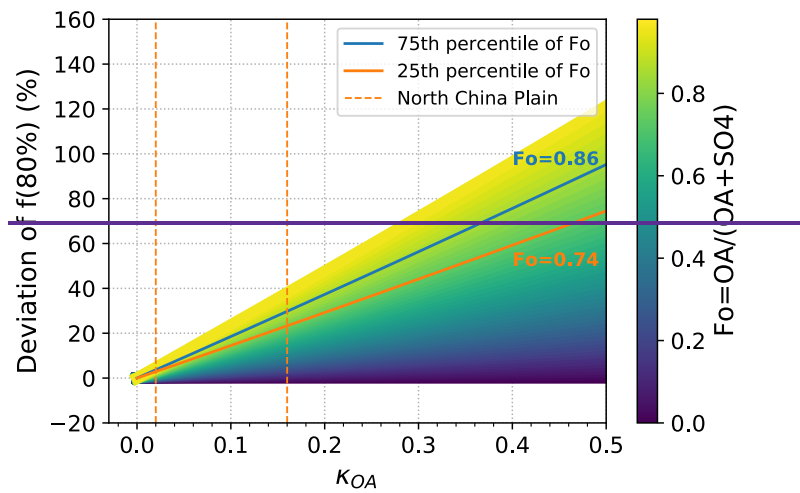
522 3.3.3 Sensitivity of aerosol scattering enhancement to κ_{OA}

523 Due to the chemical complexity of OA, the κ_{OA} values of particles are not easily
524 obtained. Various hygroscopicity parameterizations have been proposed in previous studies,
525 most of which are parameterized with chemical composition, e.g. organics or inorganics
526 fraction, and a constant assumed κ_{OA} value. Few studies consider the variation of κ_{OA} (Zhang
527 et al., 2015b; Huang et al., 2022). While these parameterizations can represent their
528 observations well, they may not be suitable for situations with different κ_{OA} values. Therefore,
529 in this section, the influence of κ_{OA} on the prediction of $f(\text{RH})$ is analyzed. We calculated the
530 $f(80\%)$ with the mean κ_{OA} in each campaign and the results are shown in Fig. 8b. The use of a
531 constant κ_{OA} average leads to a much smaller variation of the predicted $f(80\%)$ values, with
532 most of which concentrated around 1.3-1.4. Predicted $f(80\%)$ tend to overestimate lower
533 $f(80\%)$ values while underestimate higher $f(80\%)$ values. A slope of 0.50 and a R^2 of 0.01
534 indicates poor prediction in capturing the trend of $f(80\%)$. This indicates that using Fo, BCr,
535 and a constant κ_{OA} is insufficient for the prediction of $f(\text{RH})$, and that the variation of κ_{OA} need
536 to be considered, at least for situations where κ_{OA} has a large variation, such as in ORACLES.

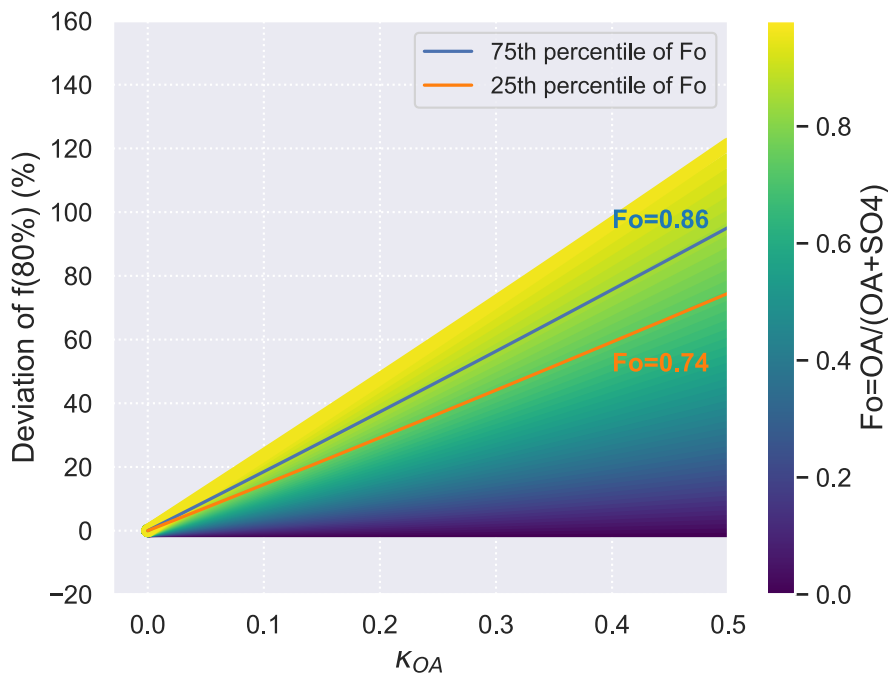
537 To quantitatively investigate the sensitivity of $f(\text{RH})$ to κ_{OA} , we calculated the deviation
538 of $f(80\%)$ with κ_{OA} for the OA-(NH₄)₂SO₄-BC mixture. The deviation of $f(80\%)$ was calculated
539 as $f(80\%, \kappa_{\text{OA}}) - f(80\%, \kappa_{\text{OA}}=0)$. As shown in Fig. 9, we observed that κ_{OA} is positively correlated
540 with $f(80\%)$. Additionally, the deviation of $f(80\%)$ is dependent on the OA fraction (Fo), i.e. a

541 higher OA fraction leads to a larger impact of κ_{OA} and consequently a larger deviation of
542 $f(80\%)$.

543 The 25th and 75th percentiles of Fo in 2016 and 2018 ORACLES campaign were 0.74
544 and 0.86, respectively. These are relatively high values and therefore result in relatively high
545 spread of $f(80\%)$. ~~Additionally As well,~~ the age of ORACLES OA spans from <4 days to > 10
546 days, during which OA oxidation and fragmentation (as discussed in Section 3.2) takes place.
547 These processes alter the hygroscopicity of OA, causing the OA in ORACLES to contribute to
548 large variations of κ_{OA} . These large variations of κ_{OA} , combined with the relatively high OA
549 fraction (Fo), makes $f(\text{RH})$ highly sensitive to the κ_{OA} value. For aerosols with a κ_{OA} of 0.4 and
550 a Fo of 0.86, the $f(80\%)$ can be 80 % higher compared to aerosols with hydrophobic OA, as
551 shown in Fig. 9. In other words, the aerosol scattering coefficients at 80 % RH are 80 % higher
552 solely because of the increase of OA hygroscopicity. This high sensitivity also explains the
553 poor prediction of $f(80\%)$ when using campaign mean κ_{OA} values, as shown in Fig. 8b. ~~We~~
554 ~~further analyzed the influence of κ_{OA} value on $f(80\%)$ for a relatively polluted site on the North~~
555 ~~China Plain based on their κ_{OA} values (Kuang et al., 2020). Its κ_{OA} rises from 0.02 in the~~
556 ~~morning to 0.16 in the noon, combining its Fo of 0.86, the $f(80\%)$ can increase by 25 % when~~
557 ~~the κ_{OA} is 0.16 compared to it being 0.02. It means that the scattering coefficients at 80 % RH~~
558 ~~can be 25 % higher at noon compared to the morning solely due to the increase of OA~~
559 ~~hygroscopicity.~~ Many studies overlook the variability of κ_{OA} and instead use a constant κ_{OA}
560 when analyzing aerosol hygroscopicity or radiative forcing. As illustrated in Fig. 9, this can be
561 reasonable when the OA fraction is low and κ_{OA} exhibits minimal variation; however, in cases
562 where these two conditions are not met, κ_{OA} can significantly influence the scattering
563 coefficients and hence direct radiative forcing.



564



565

566 Figure 9. Sensitivity of the deviation of $f(80\%)$ to κ_{OA} . The deviation of $f(80\%)$ was calculated
 567 as $f(80\%, \kappa_{OA}) - f(80\%, \kappa_{OA}=0)$. The OA to OA + SO₄ ratio (Fo) is represented by the colorbar.
 568 The blue and orange lines represent the variation at 75th and 25th percentile of Fo in both years'
 569 ORACLES campaign, respectively. The pair of dashed orange lines represent the range of κ_{OA}
 570 observed at the site on the North China Plain (Kuang et al., 2020).

571 **4 Conclusion**

572 The hygroscopicity of aerosols from the perspective of scattering enhancement over the
573 SEA Ocean during the BB season are investigated using measurements from the 2016 and 2018
574 ORACLES campaigns. The vertical distribution of aerosol hygroscopicity shows a consistent
575 pattern in both campaigns, remaining stable above 2 km; below 2 km, aerosols are more
576 hygroscopic at lower altitudes. Aerosols above 2 km have a mean and standard deviation of
577 $f(80\%)$ and $\kappa_{f(RH)}$ of 1.40 ± 0.17 and 0.19 ± 0.07 , respectively, and are less hygroscopic.
578 Conversely, aerosols below 2 km are more hygroscopic, and have a mean and standard
579 deviation of $f(80\%)$ and $\kappa_{f(RH)}$ of 1.51 ± 0.22 and 0.23 ± 0.08 , respectively, which are values at
580 the upper level of BBA hygroscopicity found in the literature. This variation of aerosol
581 hygroscopicity is consistent with the vertical variation of chemical composition. The OA and
582 sulphate mass fraction in both years show little variation above 2 km; while below this altitude,
583 OA decreases with decreasing altitude, while the sulphate mass fraction tends to increase. OA
584 oxidation through molecular fragmentation is the main mechanism for OA losses in the FT.
585 While the increase of sulphate in the MBL could indicate marine influence.

586 We retrieved κ_{OA} using Mie simulations. It shows a large variation, with the mean and
587 standard deviation being 0.11 ± 0.08 and the 25th and 75th percentiles of 0.06 and 0.16,
588 respectively. No clear relationship was found between κ_{OA} and OA oxidation level; while a
589 slight increase in κ_{OA} with volatility is shown in 2016, which may be related to the
590 fragmentation during OA oxidation, where the highly aged and low volatile OA may dissociate
591 into more volatile fragments that are still highly functionalized and hygroscopic. In all, OA
592 hygroscopicity under sub-saturated conditions can be largely influenced by solubility,
593 molecular weight, molecular functional groups, and carbon number (Cai et al., 2021; Kuang et
594 al., 2020; Rastak et al., 2017; Rickards et al., 2013; Suda et al., 2012); to better understand the
595 variation of κ_{OA} , more molecular investigations are needed.

596 In comparison with other campaigns, we find the variation of aerosol hygroscopicity in
597 the SEA is mainly due to changes in chemical composition, particularly sulphate and OA, as
598 well as variations in OA hygroscopicity during transport. To quantitatively investigate this
599 relationship, we came up with a parameterization using F_o , BC_r , and κ_{OA} , and the $f(80\%)$ from
600 Mie simulations for internally mixed OA-(NH₄)₂SO₄-BC mixture with PNSD ($D_{gn}=150$ nm
601 and $\sigma_{sg}=1.6$). This suggests that the internal mixture of OA-(NH₄)₂SO₄-BC is a good
602 approximation of aerosols with respect to the $f(RH)$ prediction in 2016 and 2018 ORACLES
603 campaign.

604 A sSensitivity study indicates that solely due to the increase in OA hygroscopicity
605 observed in our study, the aerosol scattering coefficients at 80 % RH can be amplified by 80 %.
606 Relying on the campaign's mean κ_{OA} value leads to a poor prediction of $f(80\%)$. The
607 dependence of $f(RH)$ on κ_{OA} suggests that using a constant κ_{OA} can be acceptable when the OA
608 fraction is low and κ_{OA} demonstrates limited variations. However, in situations where these
609 two conditions are not met, κ_{OA} can significantly influence the scattering coefficients and thus
610 aerosol radiative effect. Therefore, accommodating the variability of κ_{OA} is advisable.

611
612 *Competing interests.* At least one of the (co-)authors is a guest member of the editorial board
613 of Atmospheric Chemistry and Physics for the special issue “New observations and related
614 modelling studies of the aerosol-cloud-climate system in the Southeast Atlantic and southern
615 Africa regions”. The authors have no other competing interests to declare.

616
617 *Special issue statement.* This article is part of the special issue “New observations and related
618 modeling studies of the aerosol-cloud-climate system in the Southeast Atlantic and southern
619 Africa regions (ACP/AMT inter-journal SI)”. It is not associated with a conference.

620

621 *Data Availability.* Data sets are publicly available via the digital object identifier provided
622 under ORACLES Science Team reference:
623 https://doi.org/10.5067/Suborbital/ORACLES/P3/2018_V2.

624

625 *Acknowledgments.* The authors would like to thank the ORACLES team. Lu Zhang thanks the
626 postdoctoral fellowship funding from Tel Aviv University, Department of Exact Sciences.
627 Michal Segal-Rozenhaimer and Haochi Che awere supported by United States Department of
628 Energy Atmospheric System Research (ASR) grant DE-SC0020084. Caroline Dang thanks the
629 NASA Postdoctoral Fellowship Grant. Paola Formenti is supported by the AErosols, RadiatiOn
630 and CLOuds in southern Africa (AEROCLO-sA) project funded by the French National
631 Research Agency under grant agreement n° ANR-15-CE01-0014-01, the French national
632 programs LEFE/INSU and PNTS, the French National Agency for Space Studies (CNES), the
633 European Union's 7th Framework Programme (FP7/2014-2018) under EUFAR2 contract
634 n°312609, and the South African National Research Foundation (NRF) under grant UID
635 105958. The authors thank Paul Zieger for useful comments on this article.

636

637 *Financial support.* This research has been supported by the Tel Aviv University (postdoctoral
638 fellowship); the United States Department of Energy (DOE) Atmospheric System Research
639 (ASR; grant DE-SC0020084); a NASA postdoctoral fellowship; the AErosols, RadiatiOn and
640 CLOuds in southern Africa (AEROCLO-sA) project funded by the French National Research
641 Agency (grant agreement no. ANR-15-CE01-0014-01); the French national programs
642 LEFE/INSU and PNTS; the French National Agency for Space Studies (CNES); the European
643 Union's Seventh Framework Programme (FP7/2014-2018; EUFAR2 contract no. 312609); and
644 the South African National Research Foundation (NRF; grant UID 105958).

645

646

647 **References**

- 648 Alexander, B., Park, R. J., Jacob, D. J., Li, Q. B., Yantosca, R. M., Savarino, J., Lee, C. C.
649 W., and Thiemens, M. H.: Sulfate formation in sea-salt aerosols: Constraints from oxygen
650 isotopes, *J. Geophys. Res. Atmospheres*, 110, <https://doi.org/10.1029/2004JD005659>, 2005.
- 651 Andreae, M. O., Elbert, W., and de Mora, S. J.: Biogenic sulfur emissions and aerosols over
652 the tropical South Atlantic: 3. Atmospheric dimethylsulfide, aerosols and cloud condensation
653 nuclei, *J. Geophys. Res. Atmospheres*, 100, 11335–11356,
654 <https://doi.org/10.1029/94JD02828>, 1995.
- 655 Bukowiecki, N., Weingartner, E., Gysel, M., Coen, M. C., Zieger, P., Herrmann, E.,
656 Steinbacher, M., Gäggeler, H. W., and Baltensperger, U.: A Review of More than 20 Years
657 of Aerosol Observation at the High Altitude Research Station Jungfraujoch, Switzerland
658 (3580 m asl), *Aerosol Air Qual. Res.*, 16, 764–788,
659 <https://doi.org/10.4209/aaqr.2015.05.0305>, 2016.
- 660 Burgos, M. A., Andrews, E., Titos, G., Benedetti, A., Bian, H., Buchard, V., Curci, G.,
661 Kipling, Z., Kirkevåg, A., Kokkola, H., Laakso, A., Letertre-Danczak, J., Lund, M. T.,
662 Matsui, H., Myhre, G., Randles, C., Schulz, M., van Noije, T., Zhang, K., Alados-Arboledas,
663 L., Baltensperger, U., Jefferson, A., Sherman, J., Sun, J., Weingartner, E., and Zieger, P.: A
664 global model–measurement evaluation of particle light scattering coefficients at elevated
665 relative humidity, *Atmospheric Chem. Phys.*, 20, 10231–10258, [https://doi.org/10.5194/acp-](https://doi.org/10.5194/acp-20-10231-2020)
666 [20-10231-2020](https://doi.org/10.5194/acp-20-10231-2020), 2020.
- 667 Cai, M., Liang, B., Sun, Q., Liu, L., Yuan, B., Shao, M., Huang, S., Peng, Y., Wang, Z., Tan,
668 H., Li, F., Xu, H., Chen, D., and Zhao, J.: The important roles of surface tension and growth
669 rate in the contribution of new particle formation (NPF) to cloud condensation nuclei (CCN)
670 number concentration: evidence from field measurements in southern China, *Atmospheric*
671 *Chem. Phys.*, 21, 8575–8592, <https://doi.org/10.5194/acp-21-8575-2021>, 2021.
- 672 Carrico, C. M., Kus, P., Rood, M. J., Quinn, P. K., and Bates, T. S.: Mixtures of pollution,
673 dust, sea salt, and volcanic aerosol during ACE-Asia: Radiative properties as a function of
674 relative humidity, *J. Geophys. Res. Atmospheres*, 108,
675 <https://doi.org/10.1029/2003JD003405>, 2003.
- 676 Cerully, K. M., Bougiatioti, A., Hite, J. R. J., Guo, H., Xu, L., Ng, N. L., Weber, R., and
677 Nenes, A.: On the link between hygroscopicity, volatility, and oxidation state of ambient and
678 water-soluble aerosols in the southeastern United States, *Atmospheric Chem. Phys.*, 15,
679 8679–8694, <https://doi.org/10.5194/acp-15-8679-2015>, 2015.
- 680 Che, H., Zhang, X., Zhang, L., Wang, Y., Zhang, Y., Shen, X., Ma, Q., Sun, J., and Zhong, J.:
681 Prediction of size-resolved number concentration of cloud condensation nuclei and long-term
682 measurements of their activation characteristics, *Sci. Rep.*, 7, 5819,
683 <https://doi.org/10.1038/s41598-017-05998-3>, 2017.

- 684 Che, H., Segal-Rozenhaimer, M., Zhang, L., and Dang, C.: Transport and aging of biomass
685 burning aerosols in the South-eastern Atlantic Ocean, *Commun. Earth Environ.*, Accepted,
686 2021.
- 687 Che, H., Segal-Rozenhaimer, M., Zhang, L., Dang, C., Zuidema, P., Dobracki, A., Sedlacek,
688 A. J., Coe, H., Wu, H., Taylor, J., Zhang, X., Redemann, J., and Haywood, J.: Cloud
689 processing and weeklong ageing affect biomass burning aerosol properties over the south-
690 eastern Atlantic, *Commun. Earth Environ.*, 3, 182, <https://doi.org/10.1038/s43247-022-00517-3>, 2022a.
- 692 Che, H., Stier, P., Watson-Parris, D., Gordon, H., and Deaconu, L.: Source attribution of
693 cloud condensation nuclei and their impact on stratocumulus clouds and radiation in the
694 south-eastern Atlantic, *Atmospheric Chem. Phys. Discuss.*, 1–26, <https://doi.org/10.5194/acp-2022-43>, 2022b.
- 696 Chen, J., Zhao, C. S., Ma, N., and Yan, P.: Aerosol hygroscopicity parameter derived from
697 the light scattering enhancement factor measurements in the North China Plain, *Atmospheric*
698 *Chem. Phys.*, 14, 8105–8118, <https://doi.org/10.5194/acp-14-8105-2014>, 2014.
- 699 Cotterell, M. I., Willoughby, R. E., Bzdek, B. R., Orr-Ewing, A. J., and Reid, J. P.: A
700 complete parameterisation of the relative humidity and wavelength dependence of the
701 refractive index of hygroscopic inorganic aerosol particles, *Atmospheric Chem. Phys.*, 17,
702 9837–9851, <https://doi.org/10.5194/acp-17-9837-2017>, 2017.
- 703 Covert, D. S., Charlson, R. J., and Ahlquist, N. C.: A Study of the Relationship of Chemical
704 Composition and Humidity to Light Scattering by Aerosols, *J. Appl. Meteorol.*, 11, 968–976,
705 [https://doi.org/10.1175/1520-0450\(1972\)011<0968:ASOTRO>2.0.CO;2](https://doi.org/10.1175/1520-0450(1972)011<0968:ASOTRO>2.0.CO;2), 1972.
- 706 Cubison, M. J., Ortega, A. M., Hayes, P. L., Farmer, D. K., Day, D., Lechner, M. J., Brune,
707 W. H., Apel, E., Diskin, G. S., Fisher, J. A., Fuelberg, H. E., Hecobian, A., Knapp, D. J.,
708 Mikoviny, T., Riemer, D., Sachse, G. W., Sessions, W., Weber, R. J., Weinheimer, A. J.,
709 Wisthaler, A., and Jimenez, J. L.: Effects of aging on organic aerosol from open biomass
710 burning smoke in aircraft and laboratory studies, *Atmospheric Chem. Phys.*, 11, 12049–
711 12064, <https://doi.org/10.5194/acp-11-12049-2011>, 2011.
- 712 Day, D. E., Hand, J. L., Carrico, C. M., Engling, G., and Malm, W. C.: Humidification
713 factors from laboratory studies of fresh smoke from biomass fuels, *J. Geophys. Res.*
714 *Atmospheres*, 111, <https://doi.org/10.1029/2006JD007221>, 2006.
- 715 DeCarlo, P. F., Slowik, J. G., Worsnop, D. R., Davidovits, P., and Jimenez, J. L.: Particle
716 Morphology and Density Characterization by Combined Mobility and Aerodynamic
717 Diameter Measurements. Part 1: Theory, *Aerosol Sci. Technol.*, 38, 1185–1205,
718 <https://doi.org/10.1080/027868290903907>, 2004.
- 719 Ervens, B., Cubison, M., Andrews, E., Feingold, G., Ogren, J. A., Jimenez, J. L., DeCarlo, P.,
720 and Nenes, A.: Prediction of cloud condensation nucleus number concentration using
721 measurements of aerosol size distributions and composition and light scattering enhancement
722 due to humidity, *J. Geophys. Res. Atmospheres*, 112, <https://doi.org/10.1029/2006JD007426>,
723 2007.

724 Gras, J. L., Jensen, J. B., Okada, K., Ikegami, M., Zaizen, Y., and Makino, Y.: Some optical
725 properties of smoke aerosol in Indonesia and tropical Australia, *Geophys. Res. Lett.*, 26,
726 1393–1396, <https://doi.org/10.1029/1999GL900275>, 1999.

727 Gysel, M., Crosier, J., Topping, D. O., Whitehead, J. D., Bower, K. N., Cubison, M. J.,
728 Williams, P. I., Flynn, M. J., McFiggans, G. B., and Coe, H.: Closure study between chemical
729 composition and hygroscopic growth of aerosol particles during TORCH2, *Atmospheric*
730 *Chem. Phys.*, 7, 6131–6144, <https://doi.org/10.5194/acp-7-6131-2007>, 2007.

731 Haywood, J., Bush, M., Abel, S., Claxton, B., Coe, H., Crosier, J., Harrison, M., Macpherson,
732 B., Naylor, M., and Osborne, S.: Prediction of visibility and aerosol within the operational
733 Met Office Unified Model. II: Validation of model performance using observational data, *Q.*
734 *J. R. Meteorol. Soc.*, 134, 1817–1832, <https://doi.org/10.1002/qj.275>, 2008.

735 Howell, S. G., Freitag, S., Dobracki, A., Smirnow, N., and Sedlacek III, A. J.: Undersizing of
736 aged African biomass burning aerosol by an ultra-high-sensitivity aerosol spectrometer,
737 *Atmospheric Meas. Tech.*, 14, 7381–7404, <https://doi.org/10.5194/amt-14-7381-2021>, 2021.

738 Huang, S., Wu, Z., Wang, Y., Poulain, L., Höpner, F., Merkel, M., Herrmann, H., and
739 Wiedensohler, A.: Aerosol Hygroscopicity and its Link to Chemical Composition in a
740 Remote Marine Environment Based on Three Transatlantic Measurements, *Environ. Sci.*
741 *Technol.*, <https://doi.org/10.1021/acs.est.2c00785>, 2022.

742 Kacarab, M., Thornhill, K. L., Dobracki, A., Howell, S. G., O’Brien, J. R., Freitag, S.,
743 Poellot, M. R., Wood, R., Zuidema, P., Redemann, J., and Nenes, A.: Biomass burning
744 aerosol as a modulator of the droplet number in the southeast Atlantic region, *Atmospheric*
745 *Chem. Phys.*, 20, 3029–3040, <https://doi.org/10.5194/acp-20-3029-2020>, 2020.

746 Kim, J., Yoon, S.-C., Jefferson, A., and Kim, S.-W.: Aerosol hygroscopic properties during
747 Asian dust, pollution, and biomass burning episodes at Gosan, Korea in April 2001, *Atmos.*
748 *Environ.*, 40, 1550–1560, <https://doi.org/10.1016/j.atmosenv.2005.10.044>, 2006.

749 Klopper, D., Formenti, P., Namwoonde, A., Cazaunau, M., Chevaillier, S., Feron, A.,
750 Gaimoz, C., Hease, P., Lahmidi, F., Mirande-Bret, C., Triquet, S., Zeng, Z., and Piketh, S. J.:
751 Chemical composition and source apportionment of atmospheric aerosols on the Namibian
752 coast, *Atmospheric Chem. Phys.*, 20, 15811–15833, [https://doi.org/10.5194/acp-20-15811-](https://doi.org/10.5194/acp-20-15811-2020)
753 2020, 2020.

754 Kotchenruther, R. A. and Hobbs, P. V.: Humidification factors of aerosols from biomass
755 burning in Brazil, *J. Geophys. Res. Atmospheres*, 103, 32081–32089,
756 <https://doi.org/10.1029/98JD00340>, 1998.

757 Kuang, Y., Xu, W., Tao, J., Ma, N., Zhao, C., and Shao, M.: A Review on Laboratory Studies
758 and Field Measurements of Atmospheric Organic Aerosol Hygroscopicity and Its
759 Parameterization Based on Oxidation Levels, *Curr. Pollut. Rep.*, 6, 410–424,
760 <https://doi.org/10.1007/s40726-020-00164-2>, 2020.

761 Kuang, Y., Huang, S., Xue, B., Luo, B., Song, Q., Chen, W., Hu, W., Li, W., Zhao, P., Cai,
762 M., Peng, Y., Qi, J., Li, T., Wang, S., Chen, D., Yue, D., Yuan, B., and Shao, M.: Contrasting
763 effects of secondary organic aerosol formations on organic aerosol hygroscopicity,

- 764 Atmospheric Chem. Phys., 21, 10375–10391, <https://doi.org/10.5194/acp-21-10375-2021>,
765 2021.
- 766 Lambe, A. T., Onasch, T. B., Massoli, P., Croasdale, D. R., Wright, J. P., Ahern, A. T.,
767 Williams, L. R., Worsnop, D. R., Brune, W. H., and Davidovits, P.: Laboratory studies of the
768 chemical composition and cloud condensation nuclei (CCN) activity of secondary organic
769 aerosol (SOA) and oxidized primary organic aerosol (OPOA), *Atmospheric Chem. Phys.*, 11,
770 8913–8928, <https://doi.org/10.5194/acp-11-8913-2011>, 2011.
- 771 Liu, P., Song, M., Zhao, T., Gunthe, S. S., Ham, S., He, Y., Qin, Y. M., Gong, Z., Amorim, J.
772 C., Bertram, A. K., and Martin, S. T.: Resolving the mechanisms of hygroscopic growth and
773 cloud condensation nuclei activity for organic particulate matter, *Nat. Commun.*, 9, 1–10,
774 <https://doi.org/10.1038/s41467-018-06622-2>, 2018.
- 775 Liu, P. F., Zhao, C. S., Göbel, T., Hallbauer, E., Nowak, A., Ran, L., Xu, W. Y., Deng, Z. Z.,
776 Ma, N., Mildenerger, K., Henning, S., Stratmann, F., and Wiedensohler, A.: Hygroscopic
777 properties of aerosol particles at high relative humidity and their diurnal variations in the
778 North China Plain, *Atmospheric Chem. Phys.*, 11, 3479–3494, <https://doi.org/10.5194/acp-11-3479-2011>, 2011.
- 780 Liu, X. and Wang, J.: How important is organic aerosol hygroscopicity to aerosol indirect
781 forcing?, *Environ. Res. Lett.*, 5, 044010, <https://doi.org/10.1088/1748-9326/5/4/044010>,
782 2010.
- 783 Magi, B. I. and Hobbs, P. V.: Effects of humidity on aerosols in southern Africa during the
784 biomass burning season, *J. Geophys. Res. Atmospheres*, 108,
785 <https://doi.org/10.1029/2002JD002144>, 2003.
- 786 Mayer, K. J., Wang, X., Santander, M. V., Mitts, B. A., Sauer, J. S., Sultana, C. M., Cappa,
787 C. D., and Prather, K. A.: Secondary Marine Aerosol Plays a Dominant Role over Primary
788 Sea Spray Aerosol in Cloud Formation, *ACS Cent. Sci.*, 6, 2259–2266,
789 <https://doi.org/10.1021/acscentsci.0c00793>, 2020.
- 790 Mei, F., Hayes, P. L., Ortega, A., Taylor, J. W., Allan, J. D., Gilman, J., Kuster, W., de
791 Gouw, J., Jimenez, J. L., and Wang, J.: Droplet activation properties of organic aerosols
792 observed at an urban site during CalNex-LA, *J. Geophys. Res. Atmospheres*, 118, 2903–
793 2917, <https://doi.org/10.1002/jgrd.50285>, 2013.
- 794 Mie, G.: Beiträge zur Optik trüber Medien, speziell kolloidaler Metallösungen, *Ann. Phys.*,
795 330, 377–445, <https://doi.org/10.1002/andp.19083300302>, 1908.
- 796 Petters, M. D. and Kreidenweis, S. M.: A single parameter representation of hygroscopic
797 growth and cloud condensation nucleus activity, *Atmos Chem Phys*, 11, 2007.
- 798 Petters, M. D., Carrico, C. M., Kreidenweis, S. M., Prenni, A. J., DeMott, P. J., Collett, J. L.,
799 and Moosmüller, H.: Cloud condensation nucleation activity of biomass burning aerosol, *J.*
800 *Geophys. Res.*, 114, D22205, <https://doi.org/10.1029/2009JD012353>, 2009.
- 801 Quinn, P. K., Bates, T. S., Baynard, T., Clarke, A. D., Onasch, T. B., Wang, W., Rood, M. J.,
802 Andrews, E., Allan, J., Carrico, C. M., Coffman, D., and Worsnop, D.: Impact of particulate
803 organic matter on the relative humidity dependence of light scattering: A simplified
804 parameterization, *Geophys. Res. Lett.*, 32, <https://doi.org/10.1029/2005GL024322>, 2005.

805 Rastak, N., Pajunoja, A., Acosta Navarro, J. C., Ma, J., Song, M., Partridge, D. G., Kirkevåg,
806 A., Leong, Y., Hu, W. W., Taylor, N. F., Lambe, A., Cerully, K., Bougiatioti, A., Liu, P.,
807 Krejci, R., Petäjä, T., Percival, C., Davidovits, P., Worsnop, D. R., Ekman, A. M. L., Nenes,
808 A., Martin, S., Jimenez, J. L., Collins, D. R., Topping, D. o., Bertram, A. K., Zuend, A.,
809 Virtanen, A., and Riipinen, I.: Microphysical explanation of the RH-dependent water affinity
810 of biogenic organic aerosol and its importance for climate, *Geophys. Res. Lett.*, 44, 5167–
811 5177, <https://doi.org/10.1002/2017GL073056>, 2017.

812 Reddington, C. L., Morgan, W. T., Darbyshire, E., Brito, J., Coe, H., Artaxo, P., Scott, C. E.,
813 Marsham, J., and Spracklen, D. V.: Biomass burning aerosol over the Amazon: analysis of
814 aircraft, surface and satellite observations using a global aerosol model, *Atmospheric Chem.*
815 *Phys.*, 19, 9125–9152, <https://doi.org/10.5194/acp-19-9125-2019>, 2019.

816 Redemann, J., Wood, R., Zuidema, P., Doherty, S. J., Luna, B., LeBlanc, S. E., Diamond, M.
817 S., Shinozuka, Y., Chang, I. Y., Ueyama, R., Pfister, L., Ryoo, J.-M., Dobracki, A. N., da
818 Silva, A. M., Longo, K. M., Kacenelenbogen, M. S., Flynn, C. J., Pistone, K., Knox, N. M.,
819 Piketh, S. J., Haywood, J. M., Formenti, P., Mallet, M., Stier, P., Ackerman, A. S., Bauer, S.
820 E., Fridlind, A. M., Carmichael, G. R., Saide, P. E., Ferrada, G. A., Howell, S. G., Freitag, S.,
821 Cairns, B., Holben, B. N., Knobelspiesse, K. D., Tanelli, S., L’Ecuyer, T. S., Dzambo, A. M.,
822 Sy, O. O., McFarquhar, G. M., Poellot, M. R., Gupta, S., O’Brien, J. R., Nenes, A., Kacarab,
823 M., Wong, J. P. S., Small-Griswold, J. D., Thornhill, K. L., Noone, D., Podolske, J. R.,
824 Schmidt, K. S., Pilewskie, P., Chen, H., Cochrane, S. P., Sedlacek, A. J., Lang, T. J., Stith,
825 E., Segal-Rozenhaimer, M., Ferrare, R. A., Burton, S. P., Hostetler, C. A., Diner, D. J.,
826 Seidel, F. C., Platnick, S. E., Myers, J. S., Meyer, K. G., Spangenberg, D. A., Maring, H., and
827 Gao, L.: An overview of the ORACLES (ObseRvations of Aerosols above CLouds and their
828 intEractionS) project: aerosol–cloud–radiation interactions in the southeast Atlantic basin,
829 *Atmospheric Chem. Phys.*, 21, 1507–1563, <https://doi.org/10.5194/acp-21-1507-2021>, 2021.

830 Rickards, A. M. J., Miles, R. E. H., Davies, J. F., Marshall, F. H., and Reid, J. P.:
831 Measurements of the Sensitivity of Aerosol Hygroscopicity and the κ Parameter to the O/C
832 Ratio, *J. Phys. Chem. A*, 117, 14120–14131, <https://doi.org/10.1021/jp407991n>, 2013.

833 Sheridan, P. J., Jefferson, A., and Ogren, J. A.: Spatial variability of submicrometer aerosol
834 radiative properties over the Indian Ocean during INDOEX, *J. Geophys. Res. Atmospheres*,
835 107, <https://doi.org/10.1029/2000JD000166>, 2002.

836 Shingler, T., Crosbie, E., Ortega, A., Shiraiwa, M., Zuend, A., Beyersdorf, A., Ziemba, L.,
837 Anderson, B., Thornhill, L., Perring, A. E., Schwarz, J. P., Campazano-Jost, P., Day, D. A.,
838 Jimenez, J. L., Hair, J. W., Mikoviny, T., Wisthaler, A., and Sorooshian, A.: Airborne
839 characterization of subsaturated aerosol hygroscopicity and dry refractive index from the
840 surface to 6.5 km during the SEAC4RS campaign, *J. Geophys. Res. Atmospheres*, 121,
841 4188–4210, <https://doi.org/10.1002/2015JD024498>, 2016.

842 Suda, S. R., Petters, M. D., Matsunaga, A., Sullivan, R. C., Ziemann, P. J., and Kreidenweis,
843 S. M.: Hygroscopicity frequency distributions of secondary organic aerosols, *J. Geophys.*
844 *Res. Atmospheres*, 117, <https://doi.org/10.1029/2011JD016823>, 2012.

845 Sumlin, B. J., Heinson, Y. W., Shetty, N., Pandey, A., Pattison, R. S., Baker, S., Hao, W. M.,
846 and Chakrabarty, R. K.: UV–Vis–IR spectral complex refractive indices and optical
847 properties of brown carbon aerosol from biomass burning, *J. Quant. Spectrosc. Radiat.*
848 *Transf.*, 206, 392–398, <https://doi.org/10.1016/j.jqsrt.2017.12.009>, 2018.

- 849 Thompson, G. and Eidhammer, T.: A Study of Aerosol Impacts on Clouds and Precipitation
850 Development in a Large Winter Cyclone, *J. Atmospheric Sci.*, 71, 3636–3658,
851 <https://doi.org/10.1175/JAS-D-13-0305.1>, 2014.
- 852 Titos, G., Cazorla, A., Zieger, P., Andrews, E., Lyamani, H., Granados-Muñoz, M. J., Olmo,
853 F. J., and Alados-Arboledas, L.: Effect of hygroscopic growth on the aerosol light-scattering
854 coefficient: A review of measurements, techniques and error sources, *Atmos. Environ.*, 141,
855 494–507, <https://doi.org/10.1016/j.atmosenv.2016.07.021>, 2016.
- 856 Titos, G., Burgos, M. A., Zieger, P., Alados-Arboledas, L., Baltensperger, U., Jefferson, A.,
857 Sherman, J., Weingartner, E., Henzing, B., Luoma, K., O’Dowd, C., Wiedensohler, A., and
858 Andrews, E.: A global study of hygroscopicity-driven light-scattering enhancement in the
859 context of other in situ aerosol optical properties, *Atmospheric Chem. Phys.*, 21, 13031–
860 13050, <https://doi.org/10.5194/acp-21-13031-2021>, 2021.
- 861 Wang, J., Shilling, J. E., Liu, J., Zelenyuk, A., Bell, D. M., Petters, M. D., Thalman, R., Mei,
862 F., Zaveri, R. A., and Zheng, G.: Cloud droplet activation of secondary organic aerosol is
863 mainly controlled by molecular weight, not water solubility, *Atmospheric Chem. Phys.*, 19,
864 941–954, <https://doi.org/10.5194/acp-19-941-2019>, 2019.
- 865 Wang, W., Rood, M. J., Carrico, C. M., Covert, D. S., Quinn, P. K., and Bates, T. S.: Aerosol
866 optical properties along the northeast coast of North America during the New England Air
867 Quality Study–Intercontinental Transport and Chemical Transformation 2004 campaign and
868 the influence of aerosol composition, *J. Geophys. Res. Atmospheres*, 112,
869 <https://doi.org/10.1029/2006JD007579>, 2007.
- 870 van der Werf, G. R., Randerson, J. T., Giglio, L., Collatz, G. J., Mu, M., Kasibhatla, P. S.,
871 Morton, D. C., DeFries, R. S., Jin, Y., and van Leeuwen, T. T.: Global fire emissions and the
872 contribution of deforestation, savanna, forest, agricultural, and peat fires (1997–2009),
873 *Atmospheric Chem. Phys.*, 10, 11707–11735, <https://doi.org/10.5194/acp-10-11707-2010>,
874 2010.
- 875 Wu, H., Taylor, J. W., Szpek, K., Langridge, J. M., Williams, P. I., Flynn, M., Allan, J. D.,
876 Abel, S. J., Pitt, J., Cotterell, M. I., Fox, C., Davies, N. W., Haywood, J., and Coe, H.:
877 Vertical variability of the properties of highly aged biomass burning aerosol transported over
878 the southeast Atlantic during CLARIFY-2017, *Atmospheric Chem. Phys.*, 20, 12697–12719,
879 <https://doi.org/10.5194/acp-20-12697-2020>, 2020.
- 880 Zhang, L., Sun, J. Y., Shen, X. J., Zhang, Y. M., Che, H., Ma, Q. L., Zhang, Y. W., Zhang, X.
881 Y., and Ogren, J. A.: Observations of relative humidity effects on aerosol light scattering in
882 the Yangtze River Delta of China, *Atmospheric Chem. Phys.*, 15, 8439–8454,
883 <https://doi.org/10.5194/acp-15-8439-2015>, 2015a.
- 884 Zhang, L., Sun, J. Y., Shen, X. J., Zhang, Y. M., Che, H., Ma, Q. L., Zhang, Y. W., Zhang, X.
885 Y., and Ogren, J. A.: Observations of relative humidity effects on aerosol light scattering in
886 the Yangtze River Delta of China, *Atmospheric Chem. Phys.*, 15, 8439–8454,
887 <https://doi.org/10.5194/acp-15-8439-2015>, 2015b.
- 888 Zhang, L., Segal-Rozenhaimer, M., Che, H., Dang, C., Sedlacek III, A. J., Lewis, E. R.,
889 Dobracki, A., Wong, J. P. S., Formenti, P., Howell, S. G., and Nenes, A.: Light absorption by

890 brown carbon over the South-East Atlantic Ocean, *Atmospheric Chem. Phys.*, 22, 9199–
891 9213, <https://doi.org/10.5194/acp-22-9199-2022>, 2022.

892 Zhang, Q., Jimenez, J. L., Canagaratna, M. R., Allan, J. D., Coe, H., Ulbrich, I., Alfarra, M.
893 R., Takami, A., Middlebrook, A. M., Sun, Y. L., Dzepina, K., Dunlea, E., Docherty, K.,
894 DeCarlo, P. F., Salcedo, D., Onasch, T., Jayne, J. T., Miyoshi, T., Shimojo, A., Hatakeyama,
895 S., Takegawa, N., Kondo, Y., Schneider, J., Drewnick, F., Borrmann, S., Weimer, S.,
896 Demerjian, K., Williams, P., Bower, K., Bahreini, R., Cottrell, L., Griffin, R. J., Rautiainen,
897 J., Sun, J. Y., Zhang, Y. M., and Worsnop, D. R.: Ubiquity and dominance of oxygenated
898 species in organic aerosols in anthropogenically-influenced Northern Hemisphere
899 midlatitudes, *Geophys. Res. Lett.*, 34, <https://doi.org/10.1029/2007GL029979>, 2007.

900 Zieger, P., Fierz-Schmidhauser, R., Gysel, M., Ström, J., Henne, S., Yttri, K. E.,
901 Baltensperger, U., and Weingartner, E.: Effects of relative humidity on aerosol light
902 scattering in the Arctic, *Atmospheric Chem. Phys.*, 10, 3875–3890,
903 <https://doi.org/10.5194/acp-10-3875-2010>, 2010.

904 Zieger, P., Fierz-Schmidhauser, R., Weingartner, E., and Baltensperger, U.: Effects of
905 relative humidity on aerosol light scattering: results from different European sites,
906 *Atmospheric Chem. Phys.*, 13, 10609–10631, <https://doi.org/10.5194/acp-13-10609-2013>,
907 2013.

908 Zieger, P., Fierz-Schmidhauser, R., Poulain, L., Müller, T., Birmili, W., Spindler, G.,
909 Wiedensohler, A., Baltensperger, U., and Weingartner, E.: Influence of water uptake on the
910 aerosol particle light scattering coefficients of the Central European aerosol, *Tellus B Chem.*
911 *Phys. Meteorol.*, 66, 22716, <https://doi.org/10.3402/tellusb.v66.22716>, 2014.

912 Zieger, P., Aalto, P. P., Aaltonen, V., Äijälä, M., Backman, J., Hong, J., Komppula, M.,
913 Krejci, R., Laborde, M., Lampilahti, J., de Leeuw, G., Pfüller, A., Rosati, B., Tesche, M.,
914 Tunved, P., Väänänen, R., and Petäjä, T.: Low hygroscopic scattering enhancement of boreal
915 aerosol and the implications for a columnar optical closure study, *Atmospheric Chem. Phys.*,
916 15, 7247–7267, <https://doi.org/10.5194/acp-15-7247-2015>, 2015.

917